

Investigation on cellular uptake of gold nanoparticles by multiphoton laser scanning microscopy



DISSERTATION

zur Erlangung des Grades

des Doktors der Naturwissenschaften der

Naturwissenschaftlich-Technischen Fakultät III

Chemie, Pharmazie, Bio- und Werkstoffwissenschaften

der Universität des Saarlandes

von

Ke Li

Saarbrücken

2013

Tag des Kolloquiums: 22. Januar 2013
Dekan: Prof. Dr. Volkhard Helms
Berichterstatter: Jun. Prof. Dr. Marc Schneider
Prof. Dr. Gregor Jung
Vorsitz: Prof. Dr. Claus Jacob
Akad. Mitarbeiter: Dr. Qingzhong Hu

Nature shows us only the tail of the lion. But I do not doubt that the lion belongs to it even though he cannot at once reveal himself because of his enormous size.

Albert Einstein

Table of Contents

Table of Contents.....	I
1. Short Summary.....	V
2. Kurzzusammenfassung	VII
3. General Introduction.....	1
3.1. Nanoparticles for drug delivery	1
3.1.1. Principal types of nanocarriers for drug delivery	2
3.1.2. Strategies in designing nanoparticles for appropriate safety and efficiency....	3
3.2. Cellular uptake of nanoparticles	4
3.2.1. Factors influencing interactions of nano-bio interface	4
3.2.2. Phagocytic pathways of nanoparticles and relevant influencing factors	6
3.2.3. Non-phagocytic pathways of nanoparticles and relevant influencing factors	8
3.3. Technologies for imaging engulfment of nanoparticles into cells/organelles so far	10
3.4. Current problems	11
3.5. Aims of the thesis	11
3.5.1. Multiphoton absorption induced luminescence (MAIL) of different sized gold nanoparticles (AuNPs).....	12
3.5.2. AuNPs discrimination based on MAIL technique	12
3.5.3. Cellular uptake of AuNPs with various sizes	12
4. Multiphoton absorption induced luminescence of different sized AuNPs	15
4.1. Introduction.....	15
4.2. Experimental materials and methods.....	17
4.2.1. Multiphoton spectrometer system	17
4.2.2. AuNPs preparation.....	18
4.2.3. Characterization of AuNPs by TEM	19
4.2.4. Set-up to measure individual AuNPs	20
4.2.5. Single nanoparticle tracking (SPT) and verification by point spread function (PSF).....	20
4.2.6. Spectrum acquisition.....	22
4.3. Results and discussions	22

4.3.1. AuNPs morphology	22
4.3.2. Single AuNPs tracking.....	23
4.3.3. Emission intensity dependence on excitation wavelength	24
4.3.4. Spectral characteristics of AuNPs	28
4.4. Conclusions.....	32
5. AuNPs discrimination based on MAIL technique.....	35
5.1. Introduction.....	35
5.2. Experimental materials and methods.....	35
5.2.1. Nanoparticles preparation and TEM characterization.....	35
5.2.2. Cell culture and staining	36
5.2.3. Skin treatment.....	36
5.2.4. In Vitro MAIL imaging.....	37
5.3. Results and discussions	37
5.3.1. Nanoparticles morphology	37
5.3.2. Fingerprint recognition of AuNPs based on MAIL	37
5.3.3. Discrimination of AuNPs in mixed particles.....	39
5.3.4. Discrimination of AuNPs in living cells.....	40
5.3.5. Discrimination of AuNPs in skin.....	42
5.4. Conclusions.....	43
6. Cellular uptake of different sized AuNPs	45
6.1. Introduction.....	45
6.2. Materials and methods.....	47
6.2.1. Nanoparticle preparation and characterization by TEM.....	47
6.2.2. Nanoparticle quantification by UV/Vis spectroscopy	48
6.2.3. Cell culture conditions	48
6.2.4. Nanoparticle uptake	49
6.2.5. Cellular uptake dynamic of AuNPs	49
6.2.6. Confocal imaging and PSF determination.....	50
6.3. Results and discussion	51
6.3.1. AuNPs morphology	51
6.3.2. Single particle tracking of subresolution AuNPs and threshold setting	53
6.3.3. AuNPs concentration unit setting	56
6.3.4. Cellular uptake of AuNPs.....	57
6.3.5. Kinetics of particle entry.....	59
6.3.6. Cell membrane penetration ability of AuNPs.....	65
6.4. Conclusions.....	67

7. Summary	69
8. Bibliography	73
Abbreviations	81
Curriculum vitae	83
Acknowledgements	85

1. SHORT SUMMARY

Nano-based drug delivery systems (DDS) have attracted great interest recently due to the superior targeting or/and biobarriers-crossing abilities over conventional DDS. Better knowledge regarding cellular uptake behavior of nanoparticles that might be highly relevant to their cytotoxicity and physiological functions is essential. Current work in this aspect was restricted mainly due to lack of rational technique for imaging and quantification. Therefore, our aim is to pursuit a preferable approach to image and quantify the cellular uptake process of nanoparticles.

In this thesis, gold nanoparticles (AuNPs) were used as model particles. Multiphoton laser scanning microscopy was applied for exploring the cellular uptake process of AuNPs in A549 cells. The study on the multiphoton absorption induced luminescence (MAIL) of gold revealed the ongoing of the luminescence along with second harmonic generation (SHG) contributing to the final optical signal of AuNPs. By exploiting the MAIL of gold, an approach enabling simultaneous visualization and quantification of AuNPs at cellular scale was established. Experimental results in 24 h demonstrated uptake degree rising with the increase of particles size, whereas the uptake velocity showed an opposite trend.

Above results will greatly expand our previous understanding on the cellular uptake mechanism of AuNPs and will be a steady step into further exploration on the interaction of nanoparticles with cells.

2. KURZZUSAMMENFASSUNG

Drug-Delivery Systeme auf nm-Ebene haben auf Grund ihrer außergewöhnlichen Interaktion mit biologischen Barrieren in den letzten Jahren an Bedeutung gewonnen. Ein besseres Verständnis der Wechselwirkung zwischen Biosystemen und Nanopartikeln, insbesondere das Aufnahmeverhalten in Zellen ist unabdingbar. Zudem sind diese Daten relevant für die Zytotoxizität und die physiologische Funktion. Gegenwärtig existiert keine passende Abbildungs- und Quantifizierungsmöglichkeit auf nm-Ebene. Daher war Ziel dieser Arbeit einen gut nutzbaren Ansatz zum Abbilden und Quantifizieren der partikulären, zellulären Aufnahme zu entwickeln.

In dieser Arbeit wurden Goldnanopartikel (AuNP) als Modellpartikel eingesetzt. Mit Multiphoton Laser Raster Mikroskopie wurde die Aufnahme von unterschiedlich großen AuNP in A549 Zellen untersucht. Dabei wurde mit Multiphotonen Absorptions-induzierter Emission (MAIL) eine systematische Studie durchgeführt, die belegt, dass das Signal der AuNP sich aus einem Beitrag der „second harmonic generation“ (SHG) und der Lumineszenz zum optischen Gesamtsignal zusammensetzt. Mithilfe der plasmonischen Eigenschaften, war es möglich zu quantifizieren und gleichzeitig zu visualisieren. Experimente über einen 24-Stunden Zeitraum zeigten, dass größere Partikel zu einer besseren Aufnahmeeffizienz führen, während für die Aufnahme kleine Größen bevorzugt sind. Dies macht das Potenzial der Methode und der vielfältigen Einsatzmöglichkeiten von AuNP als Transportsysteme für Wirkstoffe deutlich.

3. GENERAL INTRODUCTION

3.1. NANOPARTICLES FOR DRUG DELIVERY

Since the 1950s, when biopharmaceutics and pharmacokinetics were developed, to pursue advanced drug delivery systems (DDS), for retarded and controlled release of drugs has been a major focus of attention for pharmaceutical scientists.¹ Later on, with the rapid progress of biomedical science, drug targeting to specific organs and tissues has also become one of the critical endeavors in the pharmaceutical field. Nowadays, the strategy of DDS has been regarded far more beyond a fairly simple approach to deliver therapeutic agents into the body with consistency and uniformity, but rather a powerful tool to improve the pharmacological and therapeutic properties of the “free” drugs by means of ameliorating some of their intrinsic properties such as solubility, *in vivo* stability, pharmacokinetics (PK), and biodistribution (BD).² Particularly in recent years, a great deal of novel biologically active substances with high molecular weight have been emerging continuously, including vaccines, plasmid DNA, and RNAi *etc.*, most of which are still suffering from their inherent drawbacks such as low membrane penetration ability, low selectivity of targeting aimed organelles or/and tissues, sensitivity to physiological environments and so on. Thus, to develop a desired DDS to overcome those drawbacks is imperative.

Nanoparticle-based drug carriers, being a kind of “small” DDS have attracted considerable attention from pharmaceutical scientists in the last decades. For example, the first submicronic lipid vesicle so-called liposome was reported in 1960s,³⁻⁴ followed by an increasing series of tiny drug carriers with size scale in nanometer range. These novel carriers were termed as “nanocarriers” or “nanoparticles”, possessing many crucial advantages over conventional DDS.^{1,5} For instance, by virtue of their tiny dimensions (1-1000 nm, defined for pharmaceutical purpose),¹ nanocarriers own excellent cell or tissue penetration ability rather than traditional DDS in large scale. Further, within this dimension some types of particles such as quantum dots and gold nanoparticles display unique optical properties, leading to multiple applications of these nanoparticles with respect to not only drug delivery but also imaging and labeling.⁶ As a result

of their small sizes, nanoparticles have far higher surface to mass/volume ratio relative to that of bulk materials, which enables them to adsorb, bind and carry plenty of therapeutic compounds, thus leading to high carrier capacity of drugs. Besides, capability of incorporation of both hydrophilic and hydrophobic substances, and feasibility of variable routes of administration, ranging from oral administration, inhalation, to transdermal and injection are also two main advantages of nanoparticles as drug carriers. In addition, nanoparticles can be modified to allow controlled (sustained) drug release from the matrix for various therapeutic purposes. Overall, these properties enable nanoparticles being a promising tool with considerable potential to be developed as efficient, safe, and elegant pharmaceutical carrier system to fulfill those expectations mentioned above.

3.1.1. PRINCIPAL TYPES OF NANOCARRIERS FOR DRUG DELIVERY

Nowadays, substances applied for the preparation of nanoparticles for drug delivery applications can be generally classified into two types: inorganic materials and organic materials. To be more specific, organic particles can be further defined into three species: lipid-based nanoparticles,⁷⁻⁸ polymer-based nanoparticles,⁹ and biological nanoparticles.¹⁰⁻¹³ Similarly, inorganic nanoparticles also have two types: metal-based nanoparticles¹⁴⁻¹⁹ and semiconductor nanoparticles.²⁰ In recent years, a new technology of preparing hybrid nanoparticles which comprises organic and inorganic parts has been emerging increasingly in order to achieve a multi-functional purpose.²¹⁻²³ But each part of this complex component still owns its original structures and functions similar to the pure organic or inorganic nanoparticles. Table 3.1 presents some typical types of chemical materials and possibilities for the preparation of nanoscale structures used as pharmaceutical delivery systems.

Table 3.1 Overview of the types of nanoparticles and their application in pharmaceutical sciences

Particle class	Materials	Application	Ref
Metal based	Gold	Drug/gene delivery, imaging	18, 24-27
	Ag	Antimicrobial, sensing	28-30
Semiconductor based	Silica	Drug delivery	31-32
	ZnO	Drug/gene delivery, imaging	33-36
	Magnetic iron oxide	Drug delivery	37-39
	TiO ₂	Drug delivery	40
Lipid based	Phosphatidylcholines	Drug delivery	8
Polymer based	Poly(D,L-lactic-co-glycolic)acid(PLGA)	Drug/gene delivery	41
	Polycarolactone	Drug/gene delivery	42-43
Biological materials	Albumin	Drug delivery	11-13, 44
	Chitosan	Drug delivery	45-46
	Gelatin	Drug/gene delivery	47-48
	Alginates	Drug/gene delivery	49-51

3.1.2. STRATEGIES IN DESIGNING NANOPARTICLES FOR APPROPRIATE SAFETY AND EFFICIENCY

Safety and efficiency are two crucial concerns in terms of nanoparticles used as drug carrier systems. The primary aims for designing nanocarriers for pharmaceutical applications can be summarized as following:

- Efficient and specific drug delivery and targeting,
- Suitable/tunable drug release rate at the target site,
- Reduction in toxicity and side effects from not only the drug but also the nanoparticles themselves

To realize all these aims is extremely attractive but not an easy task. Because the drug delivery efficiency and biological safety are mainly determined by a series of complex factors such as the intrinsic properties of the nanomaterials, biophysicochemical interactions at the nano-bio interface and the fate of the nanocarriers after penetration into the cells/organelles or tissues. The knowledge of those factors is basic prerequisite for the design of novel nanocarriers and is not fully understood so far. Actually, none of the existing

nanocarriers could achieve all the aspects mentioned above to the full extent. Thanks to the rapid progress in nanotechnology and some related techniques, for instance polymer-chemistry and single particle probing techniques, more and more parameters of the particles had been revealed influencing the delivery efficiency and safety with certain probability by theoretical simulation or practical experiments. Until now, enormous endeavor in design of nanocarriers with appropriate safety and efficiency had been tried, and in general they can be classified into three types: surface coating, size controlling and shape tailoring, because these three parameters dramatically impact the nanoparticles' cellular uptake behaviors that mainly determine the safety and efficiency of nanoparticles.

3.2. CELLULAR UPTAKE OF NANOPARTICLES

To make use of nanoparticles' potential for drug delivery applications, their cellular uptake behavior must be addressed because most commonly used drugs, for instance certain antimicrobial and antitumor drugs have to pass through the cell membrane before acting their functions on the subcellular sites. A series of interactions occurred at the interfaces between nanoparticles and certain biomaterials such as proteins, cells and DNA were found playing a great role in dominating the cellular uptake behavior of nanoparticles. Thus during the last decade, there has been an increasing interest in these biophysicochemical interactions at the nano-bio interface and will be described in detail later.

3.2.1. FACTORS INFLUENCING INTERACTIONS OF NANO-BIO INTERFACE

Typically, the 'nano-bio interface' is defined as the interface between nanomaterial surfaces and the surfaces of biological components such as cell membranes, organelles membranes, phospholipids, proteins and biological fluids. Numerous dynamic physicochemical interactions, kinetics and thermodynamic exchanges occur at this interface, leading to unprecedented types of complex reactions that can hardly be fully predicted by theoretical manners so far. However, investigation in the interactions at the nano-bio interface has been the most attractive aspect of nanotechnology in recent years. This knowledge is essential for us to deeply understand the cellular uptake

process of nanoparticles and to design suitable nanocarriers for the aims of drug delivery. An assembly of conceptual factors influencing interactions of nano-bio interface is summarized in Table 3.2

Table 3.2 Main biophysicochemical influences on the interface between nanomaterials and biological systems. Adopted from ⁵²

Sources of factors	Factor contents
Nanoparticles	Size, shape and surface area; Surface charge, energy, roughness and porosity; Valence and conductance states; Functional groups; Ligands; Crystallinity and defects; Hydrophobicity and hydrophilicity
Suspending media	Water molecules; Acids and bases; Salts and multivalent ions; Natural organic matter (proteins, lipids); Surfactants; Polymers; Polyelectrolytes
Solid-liquid interface	Surface hydration and dehydration; Ion adsorption and charge neutralization; Electrical double-layer formation, zeta potential, isoelectric point; Sorption of steric molecules and toxins; Electrostatic, steric and electrosteric interactions; Aggregation, dispersion and dissolution; Hydrophilic and hydrophobic interactions
Nano-bio interface	Membrane interactions: specific and nonspecific forces; Receptor-ligand binding interactions; Membrane wrapping: resistive and promotive forces; Biomolecule interactions (lipids, proteins, DNA) leading to structural and functional effects; Free energy transfer to biomolecules; Oxidant injury to biomolecules; Mitochondrial and lysosomal damage, decrease in ATP

As shown in Table 3.2, numerous characteristics of nanomaterials and biological systems have been demonstrated affecting the biophysicochemical interaction at the nano-bio interface and as well further governing the cellular uptake process of nanoparticles. However, an accurate quantitative relationship between all those parameters and the cellular uptake behavior of nanoparticles

is still unclear because of the difficulties to simultaneously manage so many variations in one experiment. In addition, the interaction between each individual parameter also requires special consideration in most of the cases. Therefore, firstly to investigate the effect of individual parameters on nanoparticles cellular uptake behavior and then collect all the assembled knowledge together could be an advisable strategy for this exploration.

3.2.2. PHAGOCYtic PATHWAYS OF NANOPARTICLES AND RELEVANT INFLUENCING FACTORS

The internalization pathway along with the intracellular fate of the nanocarrier is highly correlated with the drug release behavior in cells and further impact therapeutic effects of the drugs. Therefore, the knowledge with respect to the cell entry mechanism of nanoparticles and their relevant influencing factors is a critical issue. According to the characteristics of the particles and the properties of the cells, there are several types of mechanisms on the internalization pathway of nanoparticles. In general, they can be classified in two types: phagocytic and endocytic pathways. The latter can be further divided into four species in detail: clathrin-mediated endocytosis (CME), caveolae-mediated endocytosis (CvME), macropinocytosis and other clathrin and caveolae independent endocytosis.⁵³

Phagocytic pathway

Phagocytosis plays a great role in the uptake of nanoparticles in mammalian cells and it is mainly achieved by macrophages, monocytes, neutrophils and dendritic cells.⁵⁴ Other types of cells *e.g.* fibroblasts, epithelial and endothelial cells may also display some phagocytic activity but only to a low extent. Typically a full phagocytosis process of nanoparticle entry into cells consists of the following three steps: 1) firstly, nanoparticles are recognized by opsonization in the bio-medium or blood stream, making them 2) being apt to adhere to the macrophages and afterwards 3) ingested by macrophage cells.

Relevant nanoparticles characteristics affecting phagocytosis

- Size
- Surface properties
- Shape and rigidity

Particle size is one of the most important characteristics governing the phagocytosis. In general, the minimum size of a particle that can undergo phagocytosis is considered to be 500nm.⁵⁴ However, the experimental data from various groups often disagree with this conclusion. Some reports show that the optimum size of particles for phagocytosis is highly dependent on the particle material. For instance, polystyrene particles with sizes ranging from 250nm to 3 μ m have the optimal phagocytosis rate,⁵⁵ whereas particles smaller than 250 nm are less efficiently internalized. However, nanoparticles prepared from other polymers *e.g.* human serum albumin,⁵⁶ cellulose⁵⁷ and poly(methylmetacrylate)⁵⁶ display superior uptake efficiency with size ranging from 200nm to several microns. The reason for this disparity is still unclear and need to be further explored as well as the optimal size for other types of nanoparticles.

The surface properties of nanoparticles also play a critical role in phagocytosis by means of interacting not only with the macrophage membrane but also with opsonins. There are evidences suggesting that particles with many charges (either negatively or positively charged) and hydrophobic surface are apt to adsorb onto the opsonins rather than those particles possessing hydrophilic or non-ionic surfaces.⁵⁸⁻⁵⁹ Such properties provide an effective strategy to resist or promote phagocytosis of nanocarriers to adapt different therapeutic aims. For example, PEGylated nanocarriers display decreased reticuloendothelial systems (RES) uptake and a prolonged circulation half-life compared to their non-PEGylated counterparts after intravenous administration, resulting in a long time release of drugs.⁶⁰ On the contrary, nanocarriers coupled with some specific macrophage receptors, such as mouse monoclonal antibody dramatically enhances the phagocytosis, leading to specific targeting of drugs.⁶¹ Overall, surface functionalization provides us a powerful tool to achieve enhancement or decrease of the phagocytosis of nanoparticles.

Modification of particles' shape and rigidity gives us another option to control phagocytosis of nanoparticles. But still no clear relationship between these two factors and phagocytosis has been reported.

3.2.3. NON-PHAGOCYTTIC PATHWAYS OF NANOPARTICLES AND RELEVANT INFLUENCING FACTORS

Being different from phagocytosis only restricted to special types of cells, non-phagocytic pathways also called endocytosis, occur in all cells with the following four mechanisms: clathrin-mediated endocytosis (CME), caveolae-mediated endocytosis (CvME), macropinocytosis and other clathrin and caveolae independent endocytosis. Therefore non-phagocytic pathways have been regarded as the main dominant pathways for internalization of nanocarriers whatever the cell types and particle species.

Clathrin-mediated endocytosis (CME)

Clathrin is a type of cytosolic coat protein enriched in some regions of the cell membrane. Once exogenous particles attach to this region clathrin will be activated and form a basket-like vesicle to coat invading particles and trap them into the cell. This process is called clathrin-mediated endocytosis (CME).⁶² CME occurs in all mammalian cells and exerts a number of crucial effects particularly in nutrient uptake/exchange and intracellular communication. Previously it was believed that there was only one type of CME existing: receptor-mediated CME, but later on an alternative receptor-independent CME was also found. The common feature for these two modes can be described that both of them occur only in the membrane region where abundant clathrin is present and the destination for these endocytosed nanomaterials are the lysosomes, a place where nanoparticles undergo degradation. This property offers another strategy for aims of drug targeting or controlled release of drugs by tailoring the nanocarrier being prone to enter into cells through CME and afterwards releasing drugs in lysosomes. But this approach can only be applied to those drugs which can resist degradation by lysosomal enzymes and low pH level.

Caveolae-mediated endocytosis (CvME)

CvME is another kind of endocytic pathway identified recently.⁶³ This process often occurs on the membrane surfaces of endothelial cells, smooth muscle cells and fibroblasts that process abundant caveolin, a dimeric protein. In case

particles contact with cell surface, caveolin is stimulated to form flask-shaped membrane invagination with sizes ranging from 50nm to 100nm,^{62, 64-65} and twining the particles into cells. Unlike CME, there are no enzymes in caveolae invagination thus the particles as well as the loaded drugs can avoid enzymatic degradation. This is a great advantage for delivering drugs that are highly sensitive to enzymes such as peptides, proteins, nucleic acids, etc. Notably, the uptake velocity of CvME is much slower than that of CME.

Macropinocytosis

As another type of clathrin-independent endocytosis, macropinocytosis occurs in many cells including macrophages.⁶⁶ This process owns a mechanism similar to that of phagocytosis but offering even bigger endocytic vesicles with sizes over 1 μ m,⁶² thus can be in principle used to deliver bigger sized drug nanocarriers.

Other endocytosis pathways

Some other clathrin and caveolae independent endocytosis pathways have also been reported recently,⁶⁴ but this field is still in a very early stage and the knowledge is limited.

Relevant nanoparticles characteristics affecting endocytosis

- Size
- Surface charge and decoration
- Shape

Enormous studies have demonstrated particles size, surface properties and shape being crucial parameters governing endocytosis of nanocarriers. However, unlike phagocytosis, it is very difficult to describe a clear theoretical relationship between these properties and each type of endocytic pathway mentioned above because in most of the cases several types of endocytic mechanisms take place simultaneously, greatly disturbing observation of this aspect. Therefore, even several thousand publications have focused on the cellular uptake of nanoparticles, some basic questions such as the effect of particle size, shape and surface charge and composition on nanoparticles penetration in cells are not yet settled.⁶⁷⁻⁸¹

3.3. TECHNOLOGIES FOR IMAGING ENGULFMENT OF NANOPARTICLES INTO CELLS/ORGANELLES SO FAR

In purpose to improve the design of a nanoplatform suitable for drug delivery, using advanced imaging techniques to explore various types of cellular uptake pathways with respect to their mechanisms and corresponding influencing factors is a must. Several imaging techniques had been applied including scanning electron microscopy (SEM), transmission electron microscopy (TEM), fluorescence microscopy and surface-enhanced Raman scattering microscopy (SERS) to aid to our understanding of the cellular uptake and intracellular fate of nanoparticles.

SEM and TEM are two widely used imaging approaches in nanotechnology due to their high resolution performance. For instance, the limit of the resolution of TEM may reach 1 nm or even smaller. Previously, these two approaches were considered to be used only for detecting electron-dense particles *e.g.* metallic nanoparticles rather than those 'soft' particles with low electron density. With quick development in this field, however, advanced TEM instruments such as cryomicroscopy emerged these years enabling TEM to visualize both 'hard' and 'soft' particles.⁵² Further, recently very high resolution (resolution limit: 0.1nm, size of atom) aberration-corrected TEM instruments have been developed to image detailed atomic structures of nanoparticles. However, requirement of vacuum measurement conditions and incapability to distinguish stained cell compartments or nanoparticles being two main drawbacks limit wide applications of TEM in study of nano-bio interaction.

Fluorescently labeled nanoparticles along with corresponding optical fluorescence microscopy, for instance confocal microscopy have been successfully used to study cellular uptake behavior of various types of nanoparticles but also exhibit several problems induced by labeling approach *e.g.* instability of labeled agents, photobleaching from laser irradiation etc. Nevertheless, even with several disadvantages, fluorescence confocal microscopy along with its derivative instruments *e.g.* multiphoton laser scanning microscopy (MP-LSM) is still an irreplaceable tool for noninvasive visualization of live cell uptake of nanoparticles in real time.

Many other promising technologies have also been increasingly used to image nano-bio interaction, for example atomic force microscopy (AFM) and SERS. In general, it is very hard to judge the best one among all these techniques because each has its own advantages and shortcomings. Although bioscience community desires to develop an optimum and standard imaging approach to accomplish all measurements for nano-bio interaction, there is still a long way to go.

3.4. CURRENT PROBLEMS

As mentioned above, to understand the knowledge of cellular uptake behavior for various types of nanoparticles as well as their relevant impact factors is a crucial prerequisite for a rational design of nanoparticles-based DDS. However, some basic questions such as the effect of particles size, shape, or surface chemistry on nanoparticle uptake in cells have not been answered as a result of that many factors are not independent to each other. On the contrary, in most cases they are linked together and act simultaneously to influence the uptake process, thus greatly increasing the difficulty for scientists to judge the impact from each factor. Furthermore, although enormous effects focused on cellular uptake of nanoparticles in terms of entry pathway as well as intracellular fate of particles have been reported in recent years, few of these data can be compared directly due to discrepancy of experimental conditions applied by different research groups including various imaging and/or quantification methods, concentration units of particles *etc.*. In most cases, these data had to be normalized to a unified and suitable condition for evaluation and comparison, costing much energy but often leading to confusing conclusions. Therefore, developing a standard and unified approach enabling simultaneous visualization and quantification for cellular uptake extent of nanoparticles is necessary.

3.5. AIMS OF THE THESIS

This thesis aims to improve our understanding on the relationship between nanoparticles size and their cellular uptake behavior. Gold nanoparticles (AuNPs) are used as a model system in this aspect due to their unique optical properties, flexible size tunability, excellent biocompatibility and wide application in biomedical field.⁸²⁻⁸³ Based on multiphoton absorption induced luminescence (MAIL) of AuNPs, we established a combined 'multiphoton imaging-UV/Vis

spectroscopic analysis' method for quantitative visualization and evaluation on the cellular uptake process of AuNPs. This approach is expected to be developed as a standard tool for investigating nano-bio interactions not only for AuNPs but also for other fluorescently labeled nanoparticles. Overall, the aims of this thesis may be summarized as:

1. Investigation on the MAIL properties of AuNPs
2. Visualization and discrimination of AuNPs in complex physical and biological environments based on MAIL technique
3. Quantitative visualization and evaluation of size effect on cellular uptake of spherical AuNPs by using multiphoton imaging-UV/Vis spectroscopic analysis

3.5.1. MULTIPHOTON ABSORPTION INDUCED LUMINESCENCE (MAIL) OF DIFFERENT SIZED GOLD NANOPARTICLES (AUNPS)

In this work we mainly focused on the MAIL properties in terms of emission intensity and spectral profiles for various sized AuNPs (10-80 nm) under different excitation conditions. The MAIL of AuNPs was demonstrated to be a two photon absorption process and the pure MAIL luminescence displayed a fingerprint-like profile being independent of the irradiation conditions. This property makes MAIL a potential tool for imaging and discrimination of AuNPs in cellular uptake experiment.

3.5.2. AUNPS DISCRIMINATION BASED ON MAIL TECHNIQUE

We investigated optical properties of AuNPs after exposure to complex physical (with presence of ZnO particles) and biological environments (A549 cells and human skin) respectively. By virtue of the fingerprint-like MAIL signal, AuNPs can be easily visualized and discriminated from their counterparts (ZnO particles) and other biological tissues, proving MAIL a promising imaging tool for probing AuNPs in cells.

3.5.3. CELLULAR UPTAKE OF AUNPS WITH VARIOUS SIZES

This section addresses the cellular uptake of AuNPs with various sizes (15, 30, 50 and 80 nm) exposed to human alveolar epithelial cells (A549 cells). By exploiting of the unique MAIL profiles of AuNPs, we developed a 'multiphoton imaging-UV/Vis spectroscopic analysis' method for studying the size effect on

cellular uptake of AuNPs. This method allowed us to simultaneously visualize and quantify the cellular uptake extent of AuNPs, thus particles' uptake efficiency, dynamic and velocity can be obtained. Based on this information, the size effect on nanoparticles cellular uptake behavior can be elucidated.

4. MULTIPHOTON ABSORPTION INDUCED LUMINESCENCE OF DIFFERENT SIZED AUNPS

Abstract: Multiphoton absorption induced luminescence (MAIL), as a nonlinear optical feature of noble metallic nanoparticles has shown great advantages in the in situ detection of gold nanoparticles (AuNPs). Selection of excitation wavelengths to yield high efficient MAIL signal from different sized AuNPs is of great significance, but a systematical study of this aspect is still lacking so far. In this chapter, the optimum excitation wavelengths for visualization and discrimination of AuNPs are determined through a systematic investigation into the emission properties of AuNPs in a wide size range (10-80 nm) under multiphoton excitation with various excitation wavelengths between 710 nm and 920 nm. The emission intensity from individual particles showed excitation wavelength dependence and the superior signal to noise (S/N) ratios are obtained at excitation between 780 nm and 840 nm in wavelength. By using two generations of multiphoton microscopy (LSM-510 and LSM-710), the MAIL is confirmed a two photon absorption induced signal, along with second harmonic generation (SHG), being responsible for the visualization of AuNPs. Pure MAIL emission spectra are observed unambiguously at 900 nm excitation excluding the interference from SHG.

4.1. INTRODUCTION

With the rapid advances of modern nanoscience and nanotechnology, colloidal gold nanoparticles (AuNPs), the earliest nanomaterials used in mankind history,⁸⁴ have attracted special attention once again in physics, chemistry, biology and medicine as imaging, sensing and single particle tracking agents. The widespread use of AuNPs is due to their ease of synthesis with desired size and shape, unique optical properties and outstanding biocompatibility.^{6, 85-86} These favorable physical and chemical features along with the special property of gold surface on which facile conjugation to different functional ligands can be achieved, make AuNPs interesting carriers for drug and gene delivery.^{14-19, 22, 87-88} The rapidly growing applications of AuNPs in biomedical area, as a consequence, leads to high expectations of an ideal imaging technique

completing a convenient, characteristic, non-invasive and real time detection of gold-based nanocarriers embedded e.g. into living cells or tissue.

However, none of the existing imaging techniques fulfill all the aspects mentioned above to full extent. Many microscopy systems currently used have their own drawbacks.⁸⁹⁻⁹¹ Transmission electron microscopy (TEM) is most widely used in detecting gold, giving high resolution reaching a minimum of 1-2 nm, by means of which particles morphology could be visualized accurately. But requirement of a vacuum condition and invasive pretreatment of the samples prior to measurement restricts its application in living systems. To overcome this shortcoming, a number of established or developing imaging techniques such as second or third harmonic generation (SHG, THG), light scattering analysis and surface plasmon enhanced luminescence,⁹²⁻⁹⁵ were introduced for detecting AuNPs by exploiting the localized surface plasmon resonance (LSPR),⁹⁶ a kind of charge density oscillation confined to metallic nanoparticles under the excitation of incident light with a matching frequency that highly dependent on particles' size, shape and surface property. Lippitz *et al.*⁹⁰ reported third-harmonic generation from AuNPs, but clear signals can only be observed from particles in the range of 40-150 nm diameter. Asahi and co-workers⁹¹ recorded the scattering spectra of single gold nanoparticles interacting with living mouse fibroblasts by using a confocal Rayleigh light scattering microspectroscopy based on dark field microscopy. But low signal to noise ratio and lack of ability for deep tissue imaging, as an inevitable shortcoming of dark field microscopy, limits its full potential in this field.

Multiphoton absorption induced luminescence (MAIL), a nonlinear optical feature displayed by metallic nanoparticles upon multiphoton excitation, has been applied in imaging AuNPs in recent years. The MAIL from noble metals was firstly observed in 1969 by Mooradian.⁹⁷ In this article, MAIL was described as a process involving sequential absorption of photons and emission from the recombination of electrons in the sp-band and holes in the d-band. Following the pioneering works of Mooradian, a steady growth of knowledge in the field of MAIL from noble metals including gold was seen in the last forty years particularly in the first decade of this century.^{85, 98-100} This technique uses

excitation wavelengths in the infrared, taking advantage of lower energy of longer wavelengths, leading to reduced overall photobleaching and phototoxicity to samples and increased tissue penetration. This makes MAIL a superior alternative to other microscopy techniques in detecting gold nanoparticles in thick samples and living cells. However, the studies in this area are still in a preliminary and empirical state because some factors which determine the MAIL profiles of AuNPs are not yet well defined: the relationship between excitation wavelength and emission properties of particles, including spectral features and emission strength. Further, a number of complex but crucial questions are open: Are there any correlations between the particle size and emission intensity? Which excitation wavelength is prone to induce the highest MAIL signal from particles? Do these emission spectra display characteristic features improving their value as imaging probes? In addition, although the MAIL of noble metallic nanoparticles has been a well-known concept to all, the question how to characterize and identify these MAIL spectra, particularly with the presence of a number of interfering factors arising from complex physical or biological background is still lacking.

In this section, we systematically investigated the emission profiles of different sized AuNPs (10-80 nm) under femtosecond laser irradiation with tunable wavelengths ranging from 710 nm to 920 nm. The MAIL emission spectra of AuNPs were confirmed and characterized by comprehensive use of two generations of multiphoton laser scanning microscopy systems (MP-LSM-510 and MP-LSM-710). The impact of SHG on the presence of MAIL obtained by those two types of microscopy setups was also discussed. MAIL spectra of AuNPs exhibit fingerprint-like features, with good tolerance to complex physical and biological environments. These findings will hopefully facilitate the use of in situ imaging of AuNPs by exploiting their MAIL profiles, and benefit to further applications of AuNPs in the biomedical field.

4.2. EXPERIMENTAL MATERIALS AND METHODS

4.2.1. MULTIPHOTON SPECTROMETER SYSTEM

Figure 4.1¹⁰¹ shows a schematic illustration of the multiphoton laser scanning microscope and spectrometer system used in this study. This system consists of

three main components: 1) a conventional confocal microscopy (LSM-510 or LSM-710, Carl Zeiss, Jena, Germany), equipped with 2) a spectral detector (META, Carl Zeiss, Jena, Germany), and 3) a pulsed infrared laser (Chameleon XR, Coherent, Germany) for multiphoton excitation. The excitation source is a Ti:sapphire laser that produces sub-100-fs pulses at a repetition rate of 76MHz with tunable wavelength (specified by Coherent). The excitation light generated from the laser source is reflected by a dichroic mirror to a water immersion objective lens (Carl Zeiss: 63 \times ; 1.3 NA) and focused on the sample which is set on a XY motorized microscope stage. The emission signal is collected by the same objective and passed through the dichroic mirror along the emission path, then directed to a detection system where the CLSM image as well as corresponding emission spectra after passing a dispersing element can be obtained.

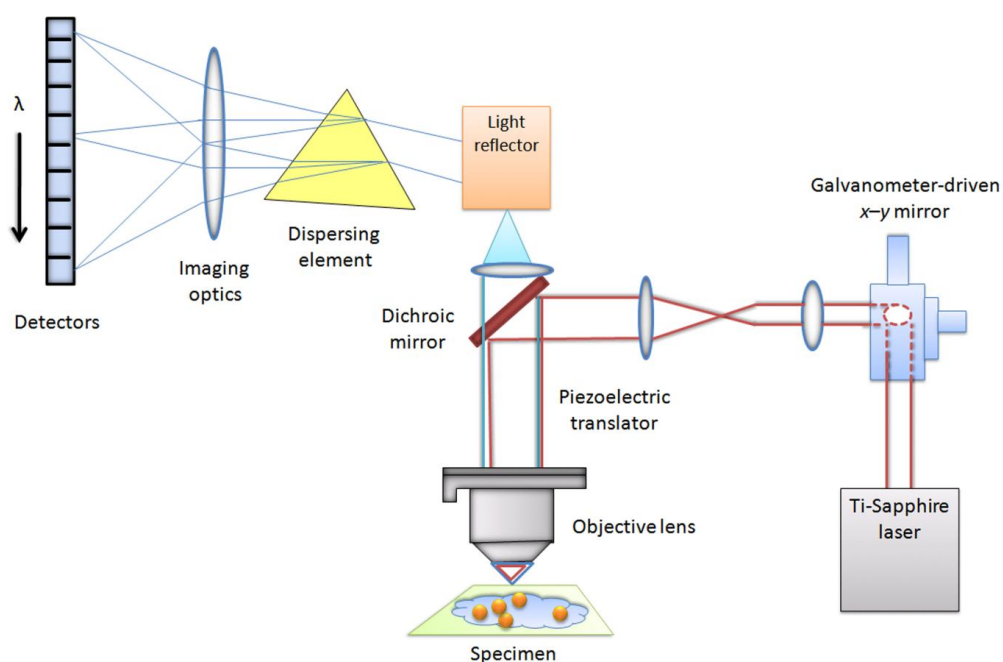


Figure 4.1. Schematic of the basic elements of a multiphoton LSM and spectrometer system (Adopted from 101)

4.2.2. AUNPS PREPARATION

Colloidal AuNPs were prepared following the method described for the first time by Turkevich *et al.* in 1951 and refined by Frens in 1972.¹⁰²⁻¹⁰³ This method is typically used to produce monodisperse spherical gold nanoparticles of around 13-20 nm in diameter. In brief, 10 mg of tetrachloroaurate ($\text{HAuCl}_4 \cdot 3\text{H}_2\text{O}$,

Sigma-Aldrich Chemie GmbH, Steinheim, Germany) was dissolved in 50 mL of ultrapure deionized water and heated to the boiling point. Then, one mL of 22.4 mg/mL aqueous solution of sodium citrate ($\text{Na}_3\text{C}_6\text{H}_5\text{O}_7 \cdot 2\text{H}_2\text{O}$, Sigma-Aldrich) was introduced under vigorous stirring to reduce the Au^{3+} to Au^0 . The solution was kept boiling for 10 minutes with sustained stirring. The resulting AuNPs were spherical with an average diameter of 18 nm. These particles were then used as gold seeds to synthesize larger AuNPs.

Because some portion of particles with unsatisfactory morphology were produced when AuNPs over 20 nm in size were synthesized by Turkevich method, a seeding growth method by Brown *et al.* was introduced to prepare larger AuNPs.¹⁰⁴ 1 mL of 18 nm AuNPs solution was diluted by ultrapure deionized water to a volume of 20 mL as gold seeds. Then, 2.1 mL of a freshly prepared aqueous solution of tetrachloroaurate (0.1%) was introduced while stirring. After 1 min, 0.358 μL hydroxylamine (NH_2OH , 50%, solution in water, Sigma-Aldrich) was quickly added to reduce the Au^{3+} . Stirring continued for 10 minutes after the color turned reddish brown. Particles prepared by this method were spherical with an average diameter of 28 nm. The water used in all experiments was prepared in a Millipore Milli-Q purification system (resistivity higher than $18.0 \text{ M}\Omega \text{ cm}^{-1}$).

Considering some non-spherical and poly-disperse particles produced as by-products on the second or third growth step, we purchased AuNPs with size of 80 nm, 50 nm and 10 nm from Ted Pella Inc (Redding, California, USA). AuNPs described above are all stabilized by citric ligands which lead to identical surface properties.

4.2.3. CHARACTERIZATION OF AUNPS BY TEM

TEM measurements of the AuNPs as well as other reference particles were performed on a JEOL model JEM 2010 instrument (JEOL GmbH, Eching, Germany) operated at an accelerating voltage of 120 kV. Samples for TEM analysis were prepared by placing 12 μL of nanoparticle solution on carbon-coated 400 mesh copper grid (S160-4, Plano GmbH, Wetzlar, Germany). The average particle diameters were obtained by measuring about 50 particles using ImageJ in an arbitrarily chosen area.

4.2.4. SET-UP TO MEASURE INDIVIDUAL AUNPS

In order to image single particles, arabic gum (Caelo, Germany) as a gel forming agent keeping particles immobilized and separated from each other, was introduced to prevent gold colloids aggregating on glass slides once exposed to air. 100 μL AuNPs was mixed with the same volume of 10% arabic gum aqueous solution under mild agitation prior to imaging. With the high viscosity of the strong gel matrix, individual particles could be fixed and distributed uniformly in the gum (Figure 4.2). In this condition, the risk of measuring aggregated particles can be decreased to a great extent. This set-up allows us to perform measurements over hours.

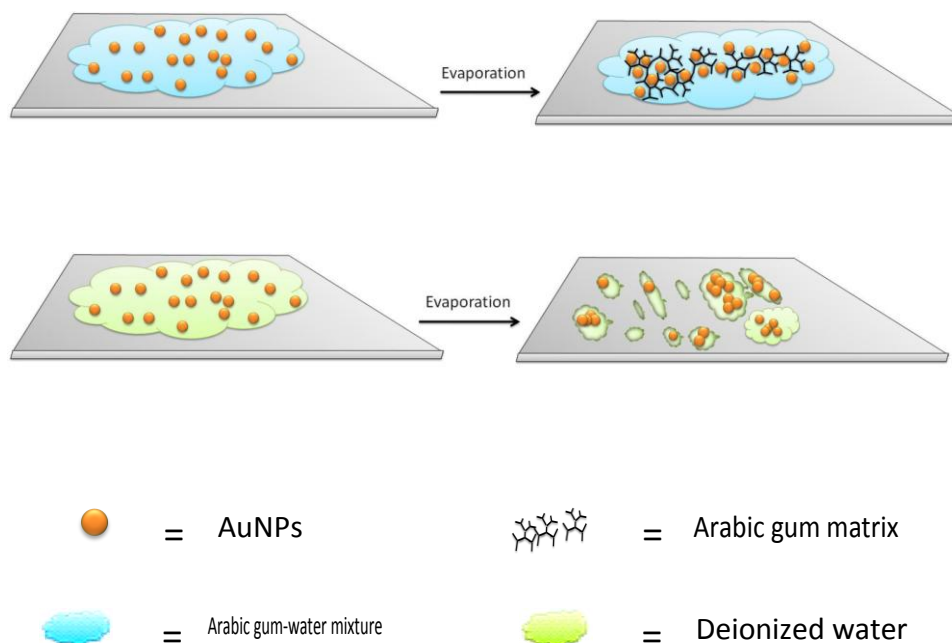


Figure 4.2. Schematic of AuNPs on a glass slide with (top panel) and without (bottom panel) the presence of arabic gum.

4.2.5. SINGLE NANOPARTICLE TRACKING (SPT) AND VERIFICATION BY POINT SPREAD FUNCTION (PSF)

AuNPs well dispersed in arabic gum were deposited dropwise on a cover slip and irradiated by a Ti:sapphire laser using a sequence of excitation wavelengths from 710-920 nm with an interval of 20 nm in 3-dimensional scanning mode. A series of such measurements were performed on different sized AuNPs. The other measurement conditions including laser power (0.485 mW), zoom (2),

gain (700) and offset (0.1) were kept identical to obtain comparable data. The output emission intensity from each single particle was recorded manually. The intensity of the peripheral area of AuNPs was also recorded by the same manner, thus the S/N ratio of particles under various excitation wavelengths can be determined. Images were acquired at a resolution of 512× 512 pixels and analyzed and edited by using the Zeiss Confocal LSM Image software, as well as ImageJ (<http://rsb.info.nih.gov/ij/download.html>).

A good hint for measuring individual AuNPs can be achieved by measuring the full width at half maximum (FWHM) for each spot. By taking advantage of the point spread functions (PSF) single gold nanoparticles can be properly verified with a high probability. FWHM of each spot can be compared to airy pattern radius of multiphoton laser scanning microscope (see Figure 4.3a).

The data of PSF measurement could be fitted to a Gaussian function by using Sigmaplot, version 12 (Systat Software GmbH, Germany) as follows:

$$f(x) = a * \exp^{-0.5\left(\frac{x-\mu}{\sigma}\right)^2} \quad (4.1)$$

Where,

a : height of the curve's peak

μ : position of the peak

σ : standard deviation.

For each function, FWHM was calculated using the following equation:

$$FWHM = 2\sigma\sqrt{2\ln 2}. \quad (4.2)$$

Typically lateral and axial resolution can be determined by measuring the FWHM of the central peak of PSF in the XY and Z directions. Based on Rayleigh criterion, individual AuNPs can be judged by comparing practically determined FWHM to theoretical lateral resolution calculated as follows:

$$r_{xy} = \frac{0.7\lambda}{NA} \quad (4.3)$$

Where, λ is the maximum light wavelength emitted from the particles and NA is the numerical aperture of the objective.

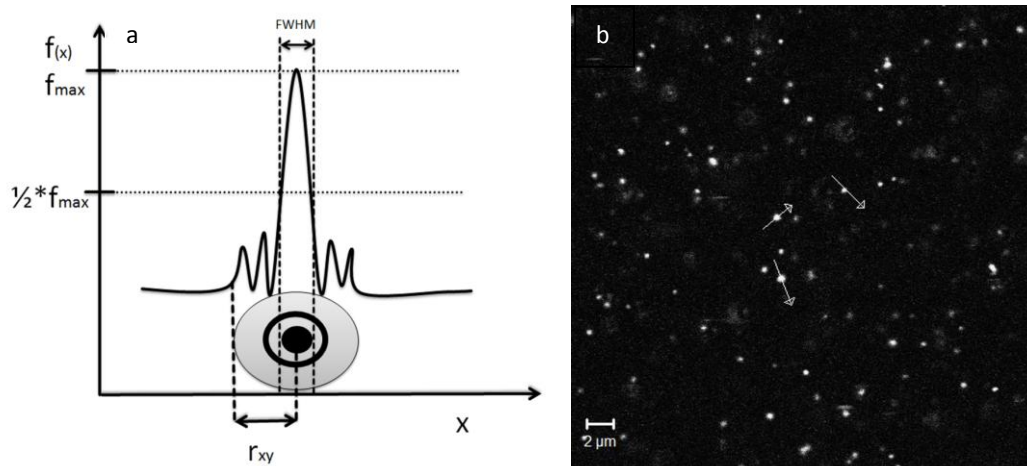


Figure 4.3. (a) Schematic of airy pattern radius and FWHM (full width at half maximum) of sub-resolution AuNPs described by PSF (point spread function). (b) Emission image of 50 nm AuNPs under excitation wavelength of 800 nm. Each bright spot represents PSF from a gold particles or cluster. By drawing an arrow cross the center of the spot, corresponding intensity distribution as a function of X axis can be presented by which FWHM could be calculated.

4.2.6. SPECTRUM ACQUISITION

With applying lambda mode (spectral analysis mode), emitted or scattered light from single particle was divided into a series of continuous wavelength bands as narrow as 10 nm over a broad wavelength range from 370 nm to 710 nm before they reached an array of separate detectors (see Figure 4.1), where the intensity of each band was measured simultaneously. By taking the signal intensity as a function of the wavelength band, the emission spectrum was acquired.

4.3. RESULTS AND DISCUSSIONS

4.3.1. AUNPS MORPHOLOGY

Representative transmission electron microscopy images (Figure 4.4) illustrate that AuNPs have a round shape and are monodisperse; quantitative analysis of particles size revealed average diameters of 10, 18, 28, 50 and 80nm respectively with standard deviation below 10%.

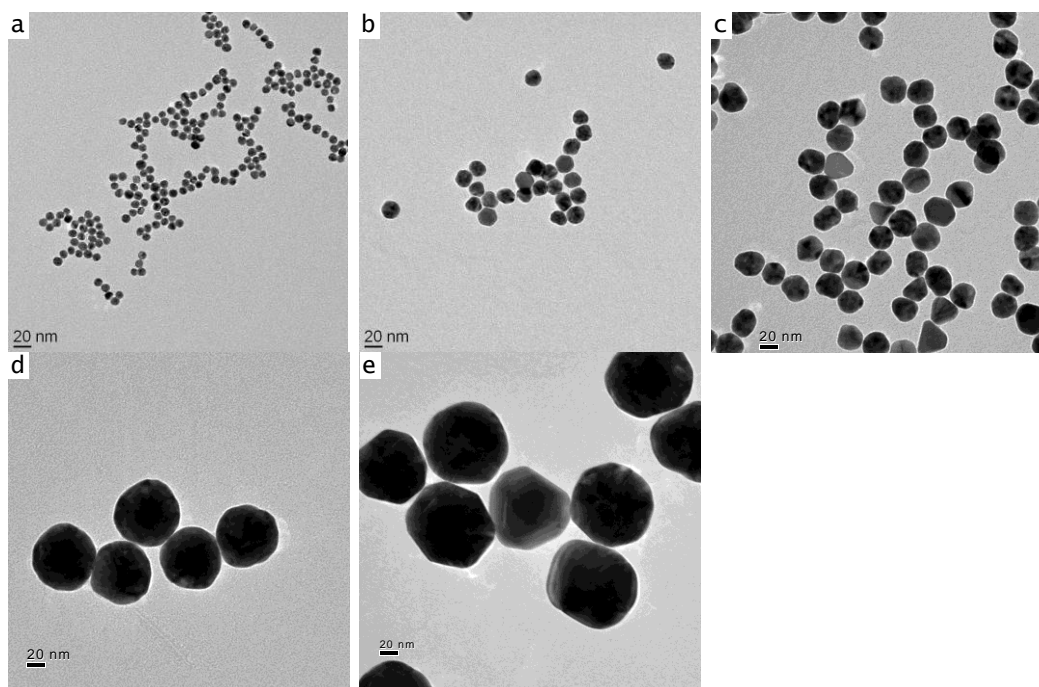


Figure 4.4. Representative transmission electron micrographs of different sized spherical AuNPs with diameters of (a-e) 10, 18, 28, 50 and 80 nm at 50,000 \times magnification.

4.3.2. SINGLE AuNPs TRACKING

By inputting relevant parameters into Equation 4.3 ($NA=1.2$, $\lambda=550\text{nm}$), the theoretical lateral optical resolution limit was calculated as 320 nm. Five representative bright spots within approximately same intensity range in the LSM images (shown in Figure 4.3b) were arbitrarily chosen for calculation of FWHM (see Table 4.1). Approximate equivalence between practically calculated FWHM and theoretical airy pattern radius indicates these AuNPs, which possess same intensity could be judged as individual with the highest probability.

Table 4.1. Comparison of practically calculated FWHM of five representative single AuNPs to theoretical airy pattern radius.

No.	FWHM(nm)	Airy pattern radius(nm)
1	327.5	
2	359.6	
3	326.8	320.8
4	332.3	
5	374.4	

4.3.3. EMISSION INTENSITY DEPENDENCE ON EXCITATION WAVELENGTH

To understand how excitation wavelength and size effects influence the MAIL efficiency of AuNPs, we irradiated different sized AuNPs homogeneously distributed in a gel and measured the emission intensity from individual particles along with their corresponding signal to noise ratio (S/N ratio) as a function of excitation wavelength, respectively. MAIL images for each sized particles were acquired by scanning the samples along the x , y and z directions. Figure 4.5 (a,b) shows representative three-dimensional MAIL images of 50 nm AuNPs. Particles were detectable in slices at all levels, suggesting their good dispersion in the solution of arabic gum. The panel images for AuNPs with other sizes were acquired and presented in Figure 4.6 a-e.

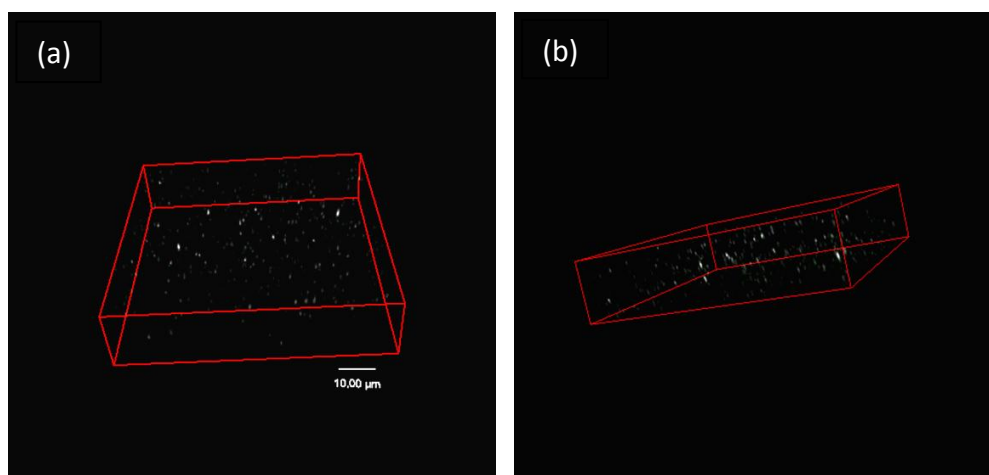


Figure 4.5. Two z-stacks as examples (a, b) for a 3-D MAIL images of 50 nm AuNPs dispersed in arabic gum at $\lambda_{ex}=800$ nm. Each white spot represents a single gold nanoparticle or possible gold aggregate.

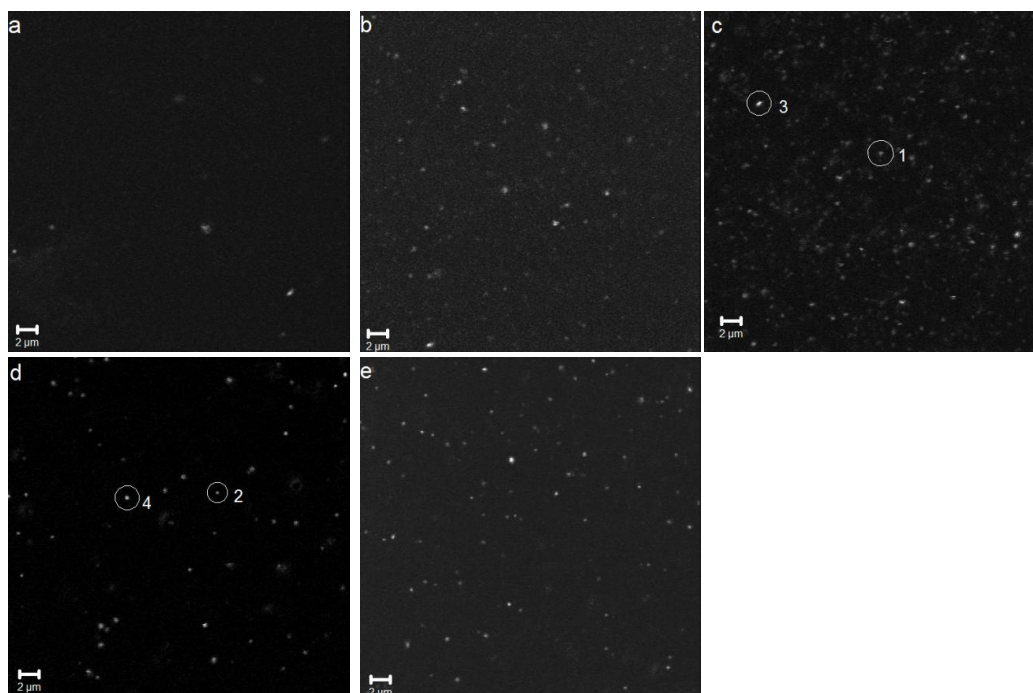


Figure 4.6. Multiphoton-LSM images of 10, 18, 28, 50 and 80 nm AuNP (a-e) dispersed in arabic gum under 800 nm excitation (laser power: 0.97 mW) display innumerable spots within the same intensity range, indicating contributions from single gold nanoparticles (e.g., spots 1 and 2). Some brighter spots which had stronger intensity in the images are assumed to be aggregates of AuNPs (such as 3 and 4).

In Figure 4.7a, the emission intensity of different sized AuNPs is plotted as a function of the excitation wavelength, showing two distinct trends. For larger particles (50 nm, 80 nm), a fast drop in emission intensity is observed from a maximum at 710nm towards longer wavelengths. On the contrary, AuNPs with diameter below 50 nm display moderate signal intensity remaining nearly constant in spite of the variation of excitation wavelengths. Since the final 'emission signals' of samples are assemble of the emitted and scattered light simultaneously collected by detectors. The difference could be interpreted in terms of the impact of the light scattering process on the emission strength of AuNPs. The detected signal is dominated by two factors: From one hand, the light scattering intensity reduces drastically with the decrease of particle size. The minimum size of which particle is able to scatter light with intensities significantly higher than other emitted signals is roughly 50 nm⁹¹ what is reflected also in our data. Due to the contribution from scattered light, AuNPs in size larger or equal to 50 nm display an optical signal with much higher intensity than those from smaller particles (10, 18 and 28 nm). The dependence

of the emission intensity on the excitation wavelength for 80 nm and 50 nm AuNPs are depicted in inset of Figure 4.7a respectively. Logarithmic plots of the emission intensity versus excitation wavelengths for 80 nm AuNPs reveals a slope of -3.86, well coinciding with Rayleigh's scattering law that the light scattering intensity is inversely proportional to the fourth power of the incident wavelength.¹⁰⁵ The slope of -2.22 for 50 nm AuNPs, however, could be interpreted in terms of a mixture of emitted luminescent light with scattered light, which is still less pronounced relative to 80 nm particles. In contrast, for AuNPs with sizes below 50 nm, their signal intensities are constant with less fluctuation regardless of the change of excitation wavelengths, indicating only slight scattering effect on small sized particles.

We also found some interfering signal coming from the matrix or substrates which exhibited intense signal as long as short excitation wavelengths (710-760 nm) were used. This holds especially true for the cover slips and glass slides. This phenomenon greatly obstructs our observation of the pure emission signal from AuNPs. To rule out this interference, S/N ratio a parameter indicating emission efficiency of AuNPs was investigated. In Figure.4.7b, a series of S/N ratio- λ_{ex} profiles for different sized AuNPs under femtosecond laser irradiation with wavelength between 710 nm and 920 nm are shown. AuNPs with 80 nm and 50 nm diameters exhibit similar profiles: S/N ratio rises from 4 at 710 nm until it reaches the highest value of 10 at 800 nm and then steadily goes down to 6 at 920 nm. This phenomenon can be explained by the fact that both the scattering effect and signal from the background reduce drastically with the increase of the excitation wavelengths from 710 nm to 800 nm. But the latter declines faster than the former, enhancing S/N ratio to a maximum at 800 nm, after which the background signal reaches a constant level whereas the scattering continues to decline, thus, reducing the S/N ratio again. Similar but less pronounced trends were also observed from the AuNPs with size below 50 nm, due to only slight scattering effects exerted on these particles. S/N ratio climbs from 4 at 710 nm to a maximum around 7 at 800 nm, and then declines again. This dependence of S/N ratio on the excitation wavelength can be assigned to different types of optical phenomenon to be responsible for the formation of total signals of AuNPs during the femtosecond laser irradiation and

will be further investigated and confirmed by spectral analysis in the next section of this study.

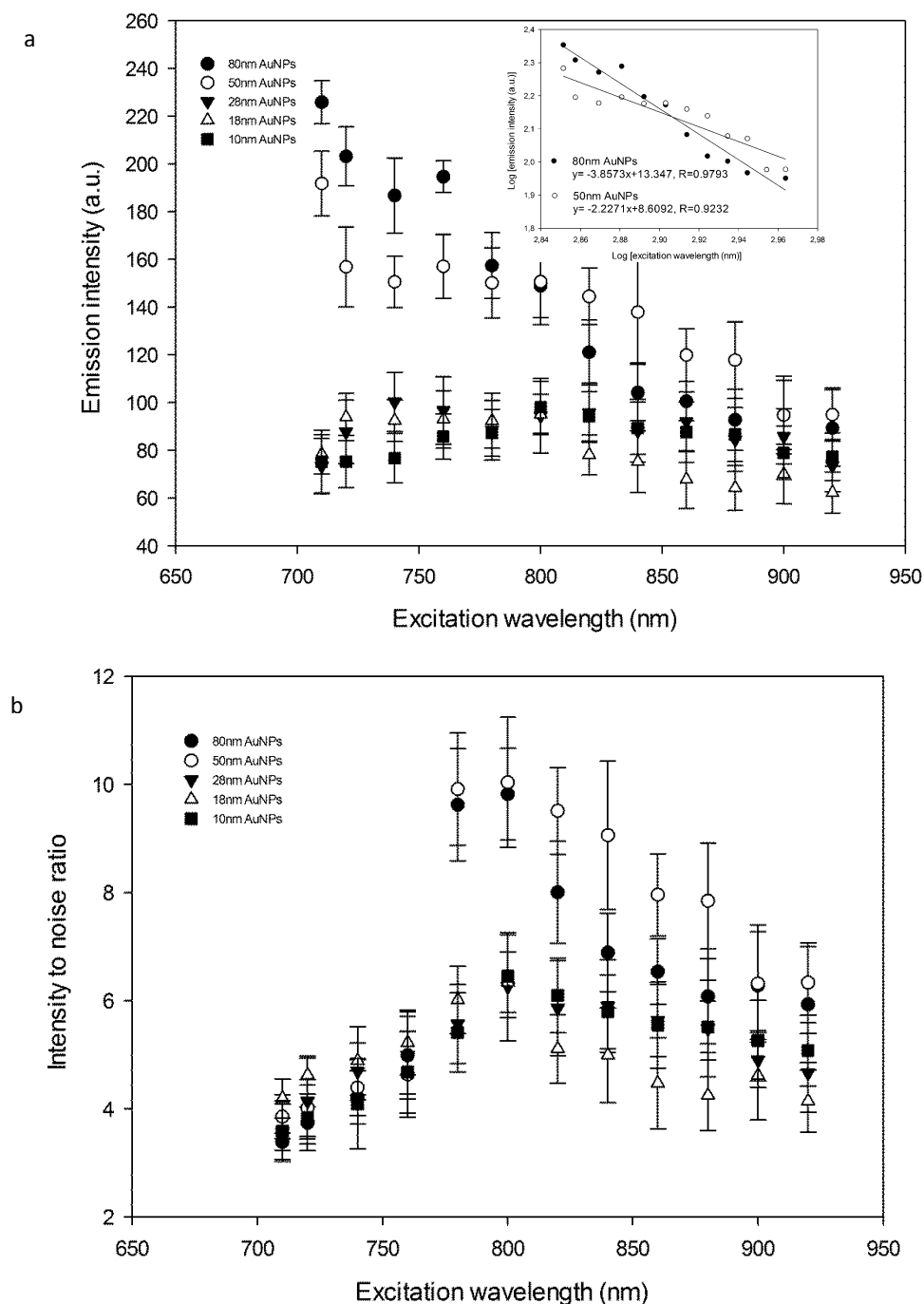


Figure 4.7 (a) Emission intensity- λ_{ex} and (b) corresponding S/N ratio- λ_{ex} profiles for different sized individual AuNPs (10, 18, 28, 50 and 80 nm). Every spot in curves represents a mean value recorded from fifteen individual particles. Inset: logarithmic plots of the emission intensity versus excitation wavelengths for 80 nm and 50 nm AuNPs along with the appropriate lines of best fit.

4.3.4. SPECTRAL CHARACTERISTICS OF AUNPS

To explore in more detail the factors causing disparity in emission efficiency of AuNPs at different excitation conditions, the characteristics of the emission spectra from AuNPs under various excitation wavelengths were analyzed and displayed in Figure 4.8 a,b respectively.

In Figure 4.8a four representative emission spectra of individual AuNPs with a diameter of 18 nm were obtained under multiphoton excitation with a series of wavelengths from 780 nm to 840 nm, due to good S/N ratio. Some common features are observed from these curves. Each spectrum approximately presents a V-shaped curve including a spectrally broad and huge tail with a width of roughly 150 nm (550-700 nm), as well as a maximum emission peak red shifting with the increase of excitation wavelength. In Figure 4.8c the measured positions of the maximum emission peak are shown as a function of the excitation wavelength changing from 780 nm to 880 nm. Obviously, the maximum peak position always locates at $\lambda_{ex}/2$, indicating a correlation to a second harmonic generation (SHG). SHG is a nonlinear light scattering process typically generated from certain type of crystals or metallic nanoparticles excited with high laser intensity. This finding is also consistent with Butet's study, in which SHG from 150 nm diameter AuNPs dispersed in gelatin was reported.⁹² In addition to the emission maximum of SHG, another typical characteristic observed in each emission line is a huge spectral tail ranging from 550 nm to 700 nm. These spectral tails display similar shapes with high intensity, making them easily distinguished from ordinary spectral peaks but their origins are still unclear and need further investigation. AuNPs with other sizes displayed similar shaped emission spectra under same excitation conditions.

To study if the same emission features can also be produced from AuNPs under different irradiation conditions, excitation at wavelengths from 860 nm to 910 nm was employed. As shown in Figure 4.8b, drastic variation of the spectrum shape is seen when for example $\lambda_{ex}=880$ nm is employed. Differing from those V-shaped spectra presented in Figure 4.8a, a mountain-like broad peak is found spreading from 500 nm to 650 nm, in addition to a maximum peak at 440 nm

induced by SHG. By continuously tuning the excitation wavelength to 900 nm and 910nm, those typical spectral tails found in Figure 4.8a are replaced by this mountain-shaped emission curves covering the full visible wavelength region from 450-650 nm. Their corresponding SHG induced maximum peaks (450 nm and 455 nm, respectively) are observed as well but less strong, making them hard to be distinguished from other ordinary peaks.

For the first time, we report excitation wavelength dependent emission profiles of AuNPs under femtosecond laser irradiation. Considering the characteristic of MAIL which is mainly described by the electronic density of AuNPs and is not expected to vary with the shift of excitation wavelength, this dependence can be explained as a number of multiple excitation mechanisms, for instance SHG and MAIL altogether being responsible for the formation of the emission signals of AuNPs. Different excitation processes dominate in different excitation wavelength region, leading to variations of the emission spectrum. The profile of each emission spectrum is an appropriate indicator with respect to its corresponding dominant excitation process which can be verified by analyzing the relationship between excitation power and emission intensity from the following equation:¹⁰⁶⁻¹⁰⁷

$$I \propto P^n \quad (4.4)$$

Where I is the integrated intensity of the emission signal, P is the laser power exerted on the sample and n is the photon number and can be experimentally calculated. With this principle the photon absorption process of AuNPs excited at different wavelengths band can be determined.

The emission intensity as a function of excitation power at 800 nm and 900 nm, respectively, as represented from the two observed behaviors, was studied. As is shown in Figure 4.8d, the logarithmic plots of the emission intensity versus laser power for 18 nm AuNPs has a slope near 2 (1.9802) at 900 nm excitation, indicating that excitation process is a two-photon absorption process. In contrast, the slope for 800 nm is close to 1 (1.1081), demonstrating a one-photon process in this case. These results show that the emission spectrum obtained at irradiation of 900 nm can be assigned to a two-photon absorption

induced luminescence (TAIL), differing from those obtained at 800 nm dominated by one photon excitation processes. These results have never been reported previously and still lack of some theoretical supports so far. However, we can interpret this phenomenon as a combination of MAIL and light scattering under femtosecond laser irradiation. These two processes may interfere with each other in most of the case, and the pure TAIL signal can only be clearly observed under irradiation at longer wavelengths range (880-910 nm) because of less pronounced light scattering at these conditions.

To further confirm the MAIL emission spectra of AuNPs, meanwhile to eliminate the interference from various types of light scattering effects, LSM-710, a new generation of multiphoton laser scanning microscope system was applied. This system is equipped with identical main components comparable to LSM-510, in addition to a novel QUASAR detector (quiet spectral array) with increased sensitivity and suppression on background noise, making it a powerful tool in trapping weak fluorescence or luminescence signals. Considering the intense SHG peak which might influence our observation on the MAIL spectra, we only recorded the emission light in range from 421 nm to 712 nm to avoid the interference from SHG. In Figure 4.9a a series of emission spectra of 18 nm AuNPs under excitation wavelengths from 780 nm to 840 nm are recorded. The emission curves acquired upon excitation of 800-840 nm exhibit typical mountain-shaped TAIL spectra with a maximum in around 500-600 nm. The absence of the big spectral tails as observed previously, indicates the independence of the TAIL profile on the excitation wavelengths as assumed. Notably, the emission spectrum obtained under 780 nm exhibits little similarity to those mountain-shaped curves but to be rather similar to the one recorded by LSM-510 at the same excitation wavelength, indicating the interference from SHG or other light scattering signals can hardly be completely eliminated even for LSM-710, particularly under irradiation with short wavelengths (710-780 nm). In Figure 4.9b, two emission curves acquired separately by LSM-510 and LSM-710 are compared under same excitation condition (900 nm). As expected, the MAIL spectrum maintains its profile regardless of the change of excitation wavelength and the type of microscope used, strongly proving the stability of MAIL as an intrinsic property of AuNPs.

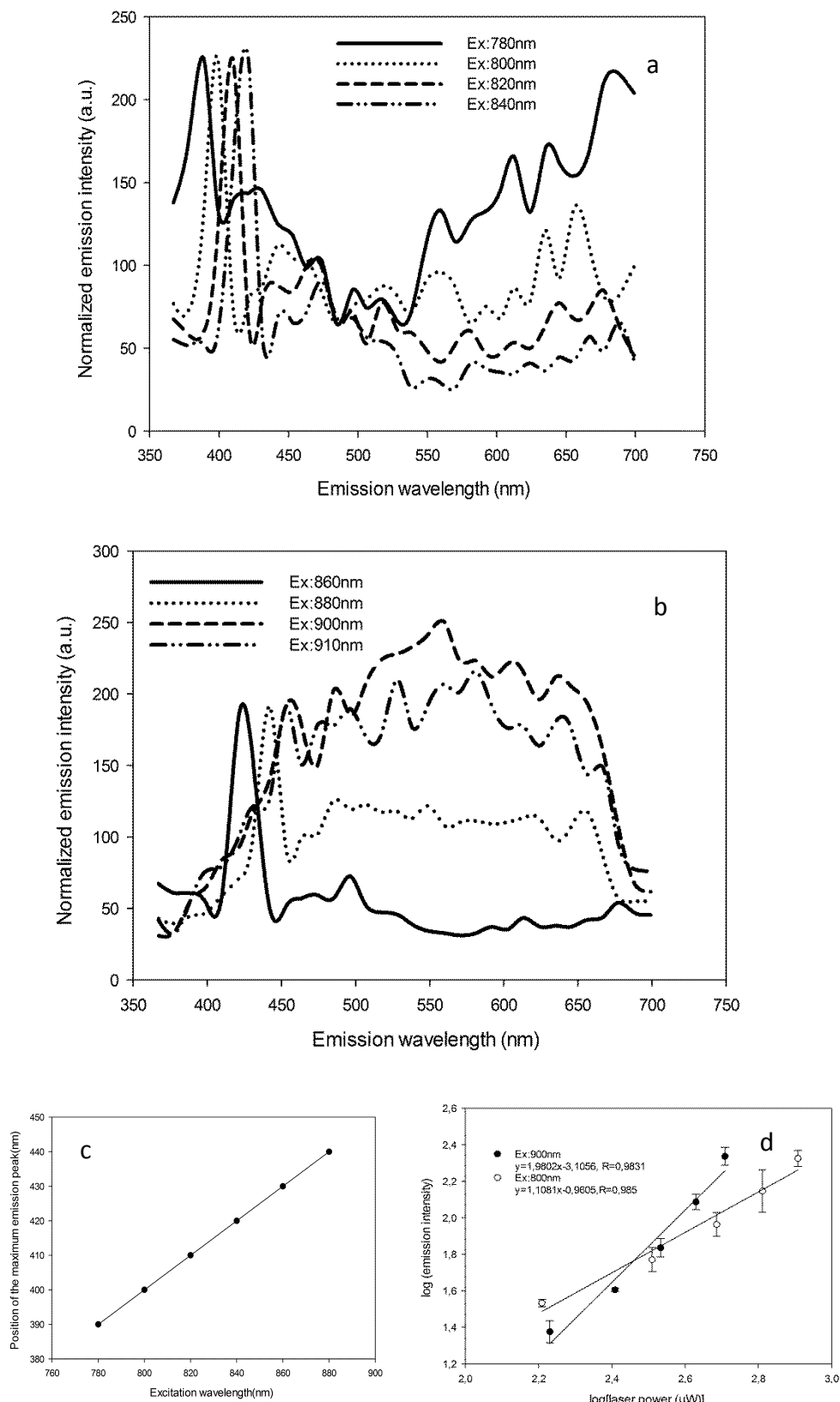


Figure 4.8. Emission spectra of individual AuNPs (18 nm) acquired by LSM-510 under various excitation wavelength of (a) 780-840 nm, (b) 860-910 nm. (c) Position of the emission maximum vs excitation wavelength. (d) Typical logarithmic plots of emission intensity vs excitation power for 18 nm AuNP at 800 nm and 900 nm excitation respectively.

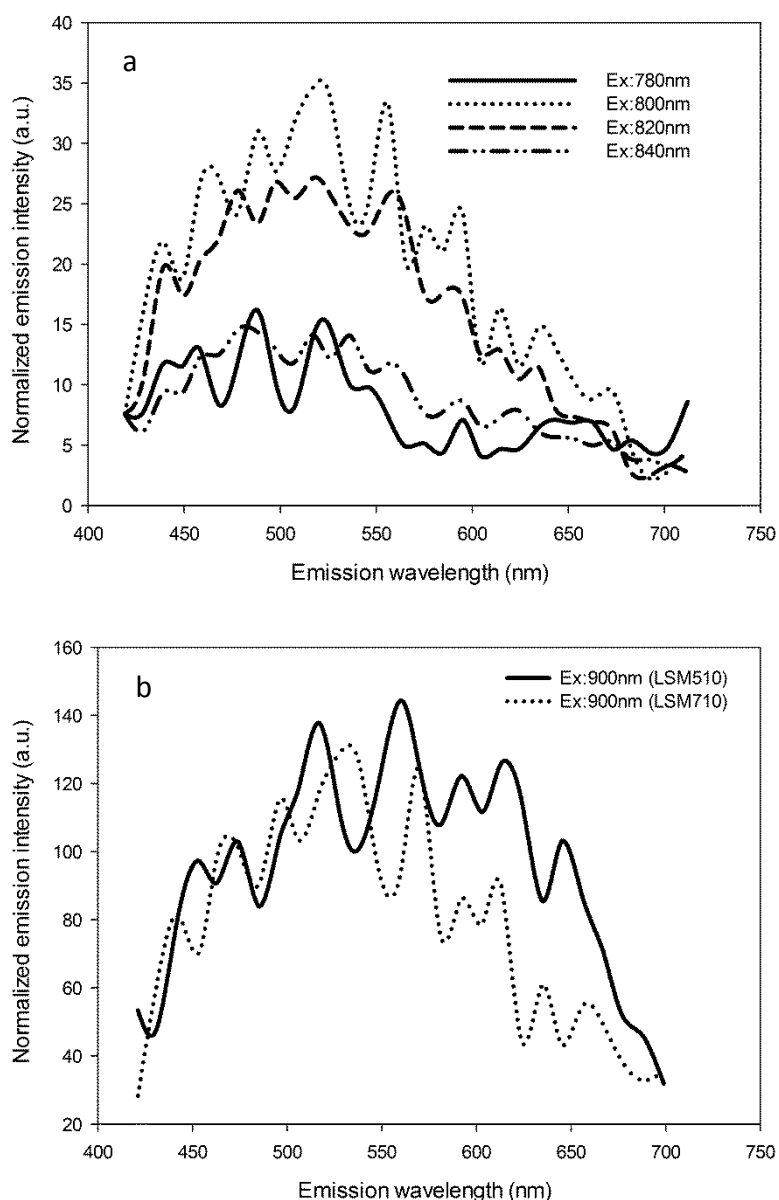


Figure 4.9. (a) Emission spectra of individual AuNPs (18 nm) acquired by LSM-710 under various excitation wavelengths from 780-840 nm. (b) Comparison of emission spectra acquired by LSM-510 and LSM-710 respectively at excitation wavelength of 900 nm.

4.4. CONCLUSIONS

Based on these results, one question raised at the beginning of this paper can be answered reasonably: It is MAIL combining with light scattering signals including SHG that contributes to the final emission profile of AuNPs. Under a broad excitation wavelength range (710-860 nm) the light scattering induced

signals show strong intensity overwhelming that from MAIL, thus greatly obstruct our observation of the MAIL. The light scattering signals show excitation wavelength dependence and gradually decrease with the growth of excitation wavelength from 710 nm until 900 nm, at which the pure MAIL spectrum of AuNPs can be easily detected without other disturbance. These conclusions were strongly supported by the emission spectra obtained and verified by using two generations of multiphoton laser scanning microscopes. The interference from the multiple scattering lights on MAIL of AuNPs was observed by use of either LSM-510 or LSM-710. Although the latter provides a relatively superior capability to detect and distinguish the real MAIL, the interference still has to be taken into account, especially in case of excitation on particles with short laser wavelengths.

5. AUNPS DISCRIMINATION BASED ON MAIL TECHNIQUE

Abstract: This chapter focuses on the visualization and discrimination of AuNPs exposed to complex physical (with presence of other semiconductor nanoparticles) or/and biological surrounding environments (living cell, human skin) by exploiting of the intrinsic MAIL profiles of gold. 900 nm excitation wavelength was applied for this purpose. In this case, fingerprint-like emission spectra were observed from AuNPs differing from ZnO and magnetic nanoparticles as well as cell organelles and skin structures, revealing a promising prospect of MAIL for identification of AuNPs in terms of in vitro cellular study.

5.1. INTRODUCTION

As described in chapter 4, AuNPs emit specific MAIL signals under femtosecond laser irradiation. These MAIL signals exhibit a potential power for AuNPs' labeling, offering superior advantages over conventional extrinsic radiotracers or fluorescence labels being apt to label instability, altered physicochemical properties and photobleaching from laser exposure. However, due to less understanding in terms of the presence of MAIL profiles of AuNPs upon various excitation wavelengths, the MAIL has not been tapped to its full potential in this aspect. In this section, 18 nm AuNPs in contact with complex physical (ZnO and magnetic nanoparticles) or/and biological environment (A549 cells and human skin) were imaged under femtosecond laser irradiation with an optimum wavelength of 900 nm, at which the specific spectra of gold can be distinguished from other species of particles as well as cells or tissues.

5.2. EXPERIMENTAL MATERIALS AND METHODS

5.2.1. NANOPARTICLES PREPARATION AND TEM CHARACTERIZATION

AuNPs were synthesized using Turkevich method as described in chapter 4. ZnO NPs (BASF, Germany) and Fe₃O₄ NPs (Chemicell, Berlin, Germany) were purchased as reference particles. All the particles were characterized by TEM (JEOL GmbH, Eching, Germany). The methodology of TEM measurement was according to 4.2.3.

5.2.2. CELL CULTURE AND STAINING

Human alveolar basal epithelial cells (A549 cells, CCL-185; ATCC, Manassas, VA, USA) were cultivated in 24-well plates (PAA Laboratories GmbH, Pasching, Austria) with a density of 2×10^4 cells per well in RPMI1640 high glucose medium supplemented with 10% heat inactivated fetal bovine serum without phenol red (PAA Laboratories GmbH, Pasching, Austria) at 37°C under 5% CO₂ atmosphere. Cells were washed three times with fresh culture medium when they reached approximately 50% confluence and then co-incubated with a gold colloidal solution diluted in fresh cell culture medium. After 6 hours incubation, cells were washed again with cell culture medium to remove loosely cell associated particles. Then the cell culture plate was set to microscopy for measurement at a condition of 37°C under 5% CO₂ atmosphere offered by a heating chamber connected with the microscopy system. Both labeled and unlabeled A549 cells associated with AuNPs were imaged respectively in this study. The staining procedure can be described as following: 10 min prior to microscopic analysis, A549 cells were again washed with PBS followed by application of Vybrant DiI (Invitrogen, Eugene, OR, USA) to bind to the cell membrane for 10 minutes at 37°C. DiI is one of the lipophilic carbocyanine analogs with $\lambda_{\text{ex}}=549$ nm and $\lambda_{\text{em}}=565$ nm. It has weak fluorescence in water but high and stable fluorescence when incorporated into membranes, making it a suitable tool for cell membrane labeling. Afterwards cells plate was immediately sent to microscopy stage for a real time investigation.

5.2.3. SKIN TREATMENT

Human skin was obtained from female patients, who had undergone abdominal plastic surgery after approval of the ethic committee of Saarland, Germany (Ärzttekammer des Saarlands, Dec.2008). The skin was cut into pieces and punched to 8mm in diameter after removal of the subcutaneous fatty tissue. Afterwards 1 mL of AuNPs solution with concentration of 100 µg/mL was dispersed on the top of skin surface and incubated for 1 h.

5.2.4. IN VITRO MAIL IMAGING

All samples prepared above were imaged by LSM-510 multiphoton laser scanning microspectroscopy (Carl Zeiss, Jena, Germany). The microscope set up and the measurement methodology was described in chapter 4.

5.3. RESULTS AND DISCUSSIONS

5.3.1. NANOPARTICLES MORPHOLOGY

Representative transmission electron microscopy images (Figure 5.1) illustrate that AuNPs have a round shape and are monodisperse. Quantitative analysis of particles size reveals average diameters of 18nm, with standard deviation below 10%. Fe₃O₄ NPs and ZnO NPs are displayed with diameters being equivalent to their spherical counterparts of 50 and 100 nm respectively.

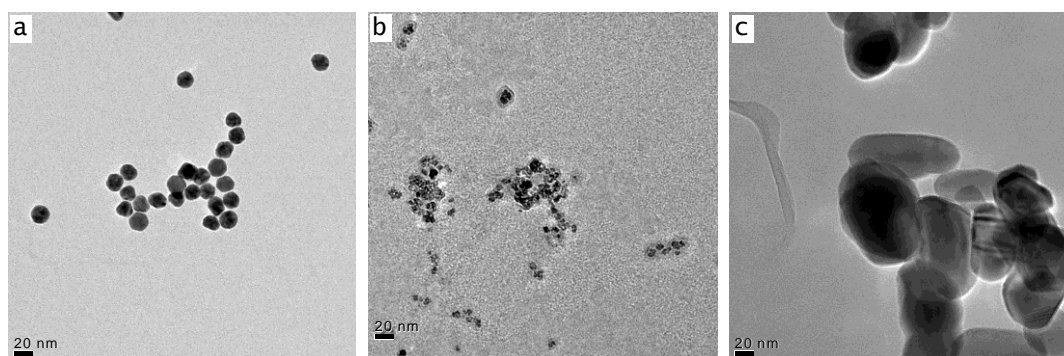


Figure 5.1. Representative transmission electron micrographs of (a) spherical AuNPs with diameters of 18 nm, (b) Fe₃O₄ NPs and (c) ZnO NPs at 50,000× magnification. The irregularly shaped Fe₃O₄ NPs and ZnO NPs were estimated to have an equal volume to that of a sphere 50 nm and 100 nm in diameter respectively.

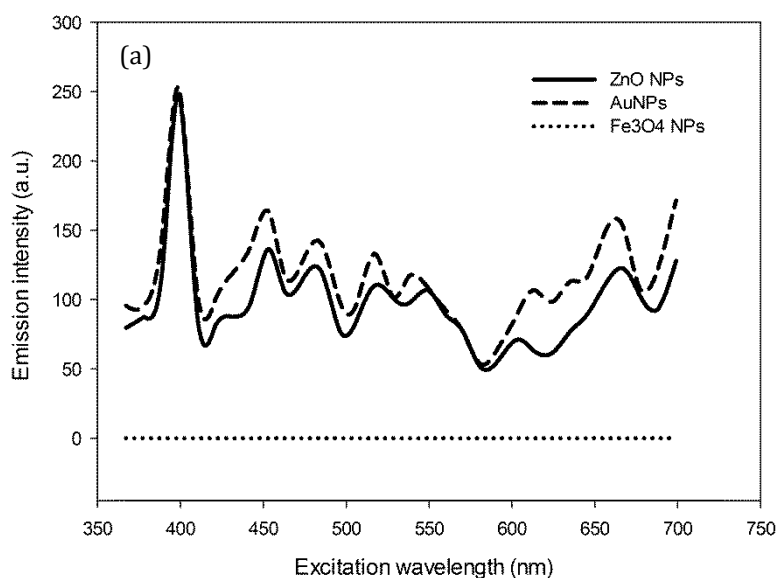
5.3.2. FINGERPRINT RECOGNITION OF AUNPS BASED ON MAIL

To verify the potential of MAIL for fingerprint recognition of AuNPs, a comparison of the emission profile between gold and two other kinds of semiconductor nanoparticles (ZnO and Fe₃O₄) was performed. These two species of particles were selected here because of their wide application in bioscience.^{33-34, 37-38}

Figure 5.2 displays a series of emission spectra recorded from AuNPs, ZnO and Fe₃O₄ irradiated at 800 nm (Figure 5.2a) and 900 nm (Figure 5.2b) respectively. Obviously, in Figure 5.2a, no signal was observed from Fe₃O₄, indicating that the electrons in Fe₃O₄ were unable to be excited by multi-photon laser. Differing

from Fe_3O_4 however, ZnO nanoparticles, a well-known SHG-producing nanomaterials,¹⁰⁸ present typical and strong SHG signal similar to gold. These spectra can be interpreted in such a way that under excitation of 800 nm, SHG dominates the emission properties of gold and ZnO nanoparticles rather than MAIL, thus causing unanimous spectra for both of them. In other words, due to less specificity in emission spectrum, gold and ZnO particles can be visualized but can hardly be discriminated from each other at 800 nm excitation.

Figure 5.2b gives emission spectra for those three types of nanoparticles by using the same microscopy setup at $\lambda = 900$ nm. Clearly, the signal from Fe_3O_4 nanoparticles are nearly at the baseline, whereas the emission characteristic of gold and ZnO now differs significantly from each other. The mountain-shaped emission spectrum from AuNPs is present as expected, that has been shown to be real MAIL. In contrast, for ZnO nanoparticles however, no remarkable spectral feature is found except for one intense peak at 450 nm as a result of SHG, implying the absence of MAIL from ZnO nanoparticles at this condition. This result shows the ability to discriminate AuNPs in a complex physical environment, from other nanoparticle species.



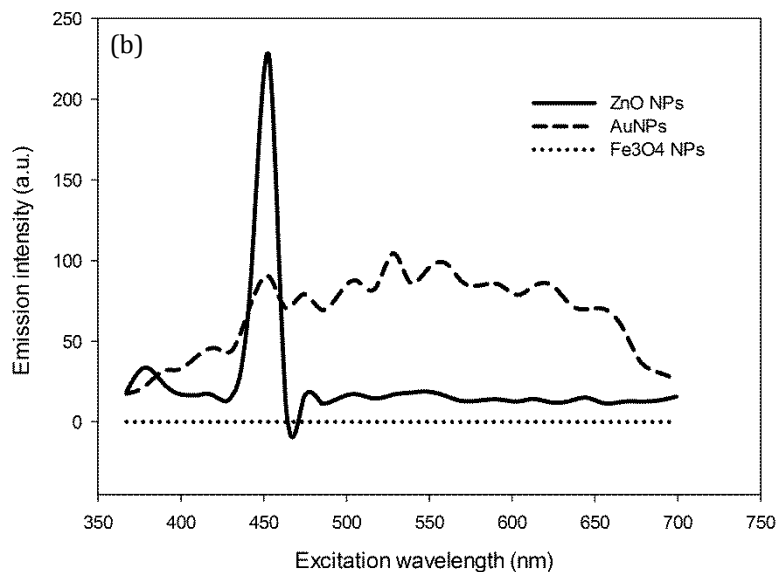


Figure 5.2. Emission spectra of individual gold, ZnO, and Fe₃O₄ nanoparticles acquired at (a) 800 nm, (b) 900 nm excitation wavelengths.

5.3.3. DISCRIMINATION OF AuNPs IN MIXED PARTICLES

To support this potential of MAIL for AuNPs discrimination, a mixture of gold and ZnO nanoparticles was imaged under multiphoton excitation at 900 nm. A conventional MAIL image (Figure 5.3a) along with its corresponding image in lambda mode (Figure 5.3b) recorded on the same sample section is shown.

As seen from Figure 5.3a, each red spot representing mixed particles expresses strong MAIL and/or SHG signals. These multiple signals can be exclusively assigned to their origin by taking advantage of balancing the images by their spectrum. In Figure 5.3b, signals being responsible for the visibility of gold or ZnO are easily identified due to the unique MAIL and SHG features. Blue color signals can be considered generated from ZnO nanoparticles supported by its corresponding emission spectrum, a typical SHG spectrum shown in Figure 5.3c. Spots with red color, on the contrary, are originating from the broad, gold – typical MAIL emission.

Notice the spectrum shape does not precisely match that from pure AuNPs observed previously. The spectrum is narrowed by around 150 nm and the intensity maximum is red-shifted by 100 nm to 650 nm. This difference is assumed as a result of the electron interaction between gold and ZnO closely located influencing the polarization state of electrons on the gold surface, thus leading to MAIL spectrum change. Nevertheless, the spectrum of gold still keeps

its overall fingerprint-like characteristic and can be easily discriminated from the emission curve of ZnO, indicating great potential for characterization or identification of AuNPs in a complex physical environment.

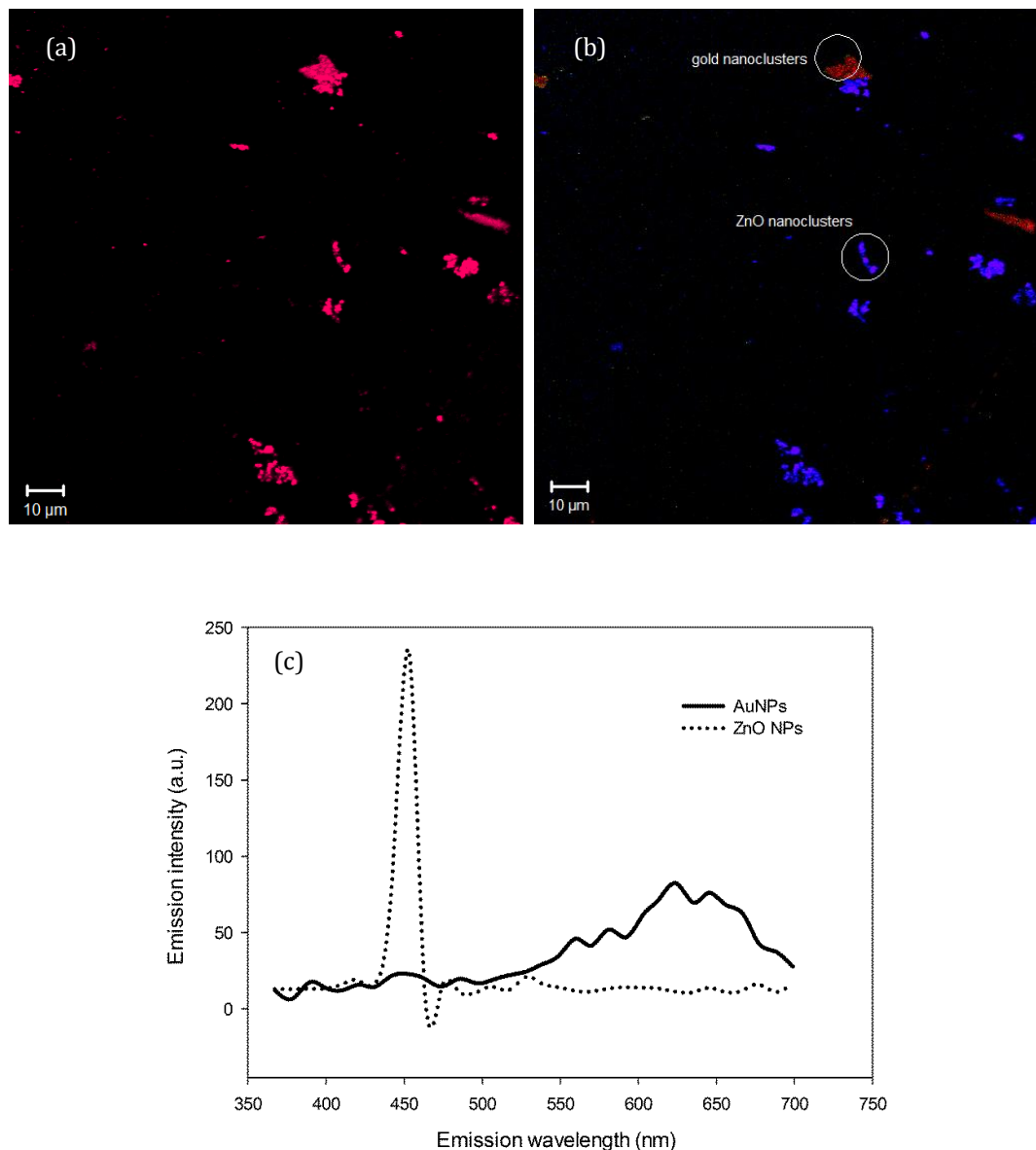


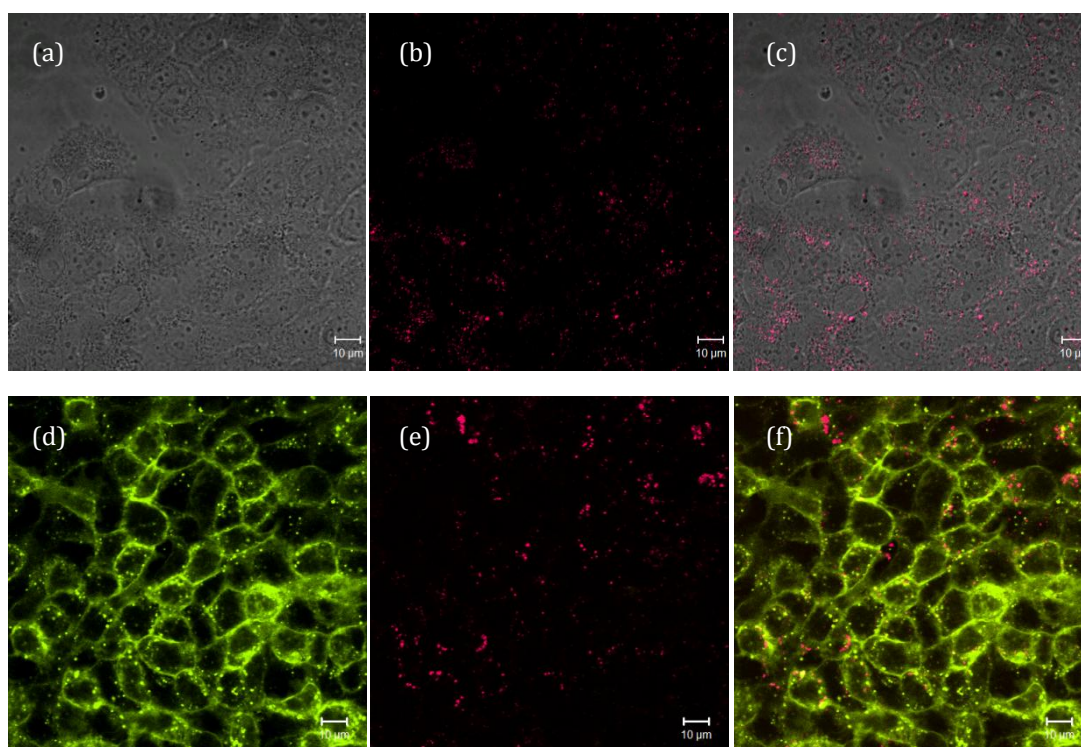
Figure 5.3. Multiphoton spectral images of a gold and ZnO nanoparticles mixture in (a) false color and (b) true color representation. And (c) the corresponding emission spectra of gold and ZnO at 900nm excitation.

5.3.4. DISCRIMINATION OF AUNPS IN LIVING CELLS

In order to determine the impact of complex biological environment on the MAIL profile of AuNPs, unlabeled and DiI labeled living A549 cells coincubated with 18 nm AuNPs were imaged.

The measurement is performed in a multi-track mode consisting of two tracks: one is 'cell track' involving a transmittance mode to image unlabeled cells and a fluorescence channel for DiI labeled cells ($\lambda_{\text{ex}}=543$ nm) with a set of BP 560-615 nm filters to collect the emission signals from cell membrane; the other is 'gold track' for imaging AuNPs at $\lambda_{\text{ex}}=900$ nm along with a KP 660 nm filter to track gold.

As is shown in Figure 5.4 a-f, bright MAIL signals represented as red spots are emitted from AuNPs embedded in cells without interference from the presence of cells and cell organelles. No signal crosstalk is found between labeled cells and AuNPs illustrated by their corresponding emission spectra in Figure 5.4 g. Spectral analysis presents the typical MAIL spectrum from AuNPs differing from those of unlabeled and labeled cells, revealing that the bio-environmental influence on the MAIL profiles of gold can be neglected. These results prove good efficiency and stability of the fingerprint-like MAIL spectra of AuNPs under complex bio-environments. The cells endured the illumination for several hours with their original morphologies and grew to 90% confluency over night after measurement, showing tolerability under this measurement condition. From these results we can conclude MAIL as a feasible probe for imaging AuNPs in living cells.



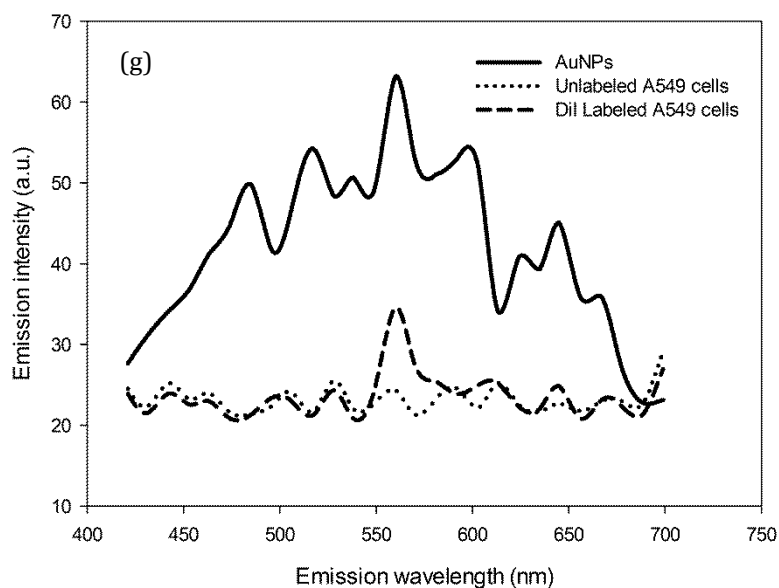


Figure 5.4. Multitracking images of 18 nm AuNPs incubated with (a-c) unlabeled and (d-f) labeled A549 cells, (g) along with the corresponding emission spectra of AuNPs and cell membrane at 900 nm excitation. Transmittance channel (grey scale, 543 nm excitation), fluorescence channel (green scale, 543 nm excitation), MAIL channel (red scale, 900 nm excitation), and color overlay images are provided. Green denotes the cell contour (DiI label for plasma membrane), while red indicates AuNPs.

5.3.5. DISCRIMINATION OF AuNPs IN SKIN

To further evaluate the stability and sensitivity of MAIL from AuNPs in contact with thick and dense tissue, which is apt to produce strong autofluorescence under visible light excitation causing interference on the presence of signal from particles, human skin is introduced here to imitate a difficult environment and treated with AuNPs for evaluation. Figure 5.5a-c presents a series of multi-track images of a piece of human skin following exposure to 18 nm AuNPs 30 min, consisting of a multiphoton image at 900 nm excitation for tracking AuNPs, a conventional fluorescence image excited at 543 nm for detecting skin, as well as an overlay of them. As evidenced by the MAIL image, AuNPs can be observed associated with dermal layer which is indicated by its autofluorescence generated at 543 nm excitation, under which no gold signal presents. Back to the 'gold track', however, only bright MAIL signals from AuNPs are displayed without the presence of autofluorescence signal from skin, because the MAIL efficiency of AuNPs is far higher than the autofluorescence from skin excited in this case confirmed by the MAIL image and corresponding emission spectra shown in Figure 5.5d. Spectra analysis gives a typical MAIL spectrum of AuNPs

with intense intensity and an autofluorescence spectrum of skin with intensity closing to background level, suggesting high stability and sensitively of MAIL from AuNPs deep into skin. These findings enable us to confirm the potential of MAIL for imaging applications of gold based nanocarriers in percutaneous drug delivery field.

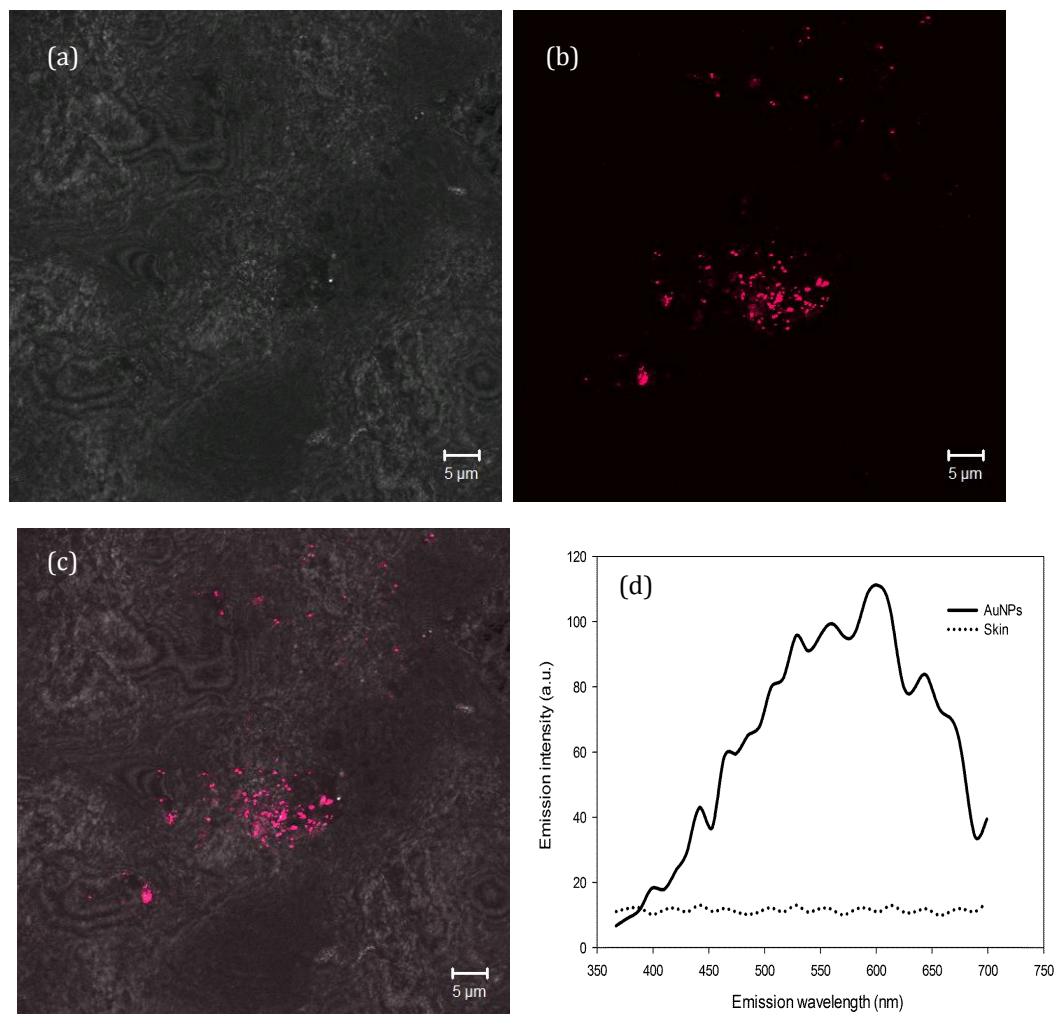


Figure 5.5. Multitracking images of 18 nm AuNPs incubated with human skin (a,b,c) and (d) corresponding emission spectra of AuNPs and skin at 900 nm excitation respectively. A skin channel (grey scale, 543 nm excitation), a gold channel (red scale, 900 nm excitation) and color overlay images are provided. All images are from the same field of a view.

5.4. CONCLUSIONS

In conclusion, the optimum excitation wavelength for discrimination of AuNPs is 900 nm, upon which fingerprint-like MAIL spectrum can be easily detected without interference from SHG. This emission spectrum shows high stability and specificity, enabling us to use this feature as a fingerprint to identify and discriminate AuNPs in complex physical or biological environments, for instance

living cells and/or other particles. Thus, a standard protocol for in situ visualization and discrimination of AuNPs in complex surrounding physical and physiological environments can be established. We describe this process as the following two steps: (i) samples is illuminated by laser using optimum wavelengths ranging from 780 nm to 840 nm, within which clear emission signals of particles with superior S/N ratio can be obtained. For the aims of identify and discriminate AuNPs from other coincubated particles or biotissue, (ii) excitation wavelength is further shifted to 900 nm under which the fingerprint-like MAIL spectrum can be detected as a self labeling probe. These advantages of MAIL technique over other imaging approach with respect to safety, efficiency, specificity and deep tissue penetration capability will be useful for in situ visualization and discrimination of those AuNPs-based drug/gene nanocarriers in biomedical or pharmaceutical fields.¹⁰⁹⁻¹¹¹

6. CELLULAR UPTAKE OF DIFFERENT SIZED AUNPS

Abstract: With wide applications of nanoscale materials in biomedical field, the impact of nanoparticle size on its cellular uptake efficiency, dynamics and mechanism has attracted numerous interests but the knowledge in this aspect is still a matter of controversy. In this study a combined “multiphoton imaging-UV/Vis spectroscopic analysis” method was applied for the first time for quantitative visualization and evaluation on the cellular uptake process of different sized (15, 30, 50, and 80 nm) AuNPs. This technique enables quantitative analysis of the size effect on cellular uptake behavior of AuNPs from a stack of 3D multiphoton laser scanning microscopy (MP-LSM) images meanwhile provides a capability for differentiating AuNPs present in external and internal subcellular components (cell membrane and cytoplasm) respectively, giving detailed information for better elucidating the cellular uptake mechanisms and dynamics. The data shows the internalization extent of AuNPs is highly dependent on particles sizes and incubation time. Due to the sedimentation effect, 50 and 80 nm AuNPs are taken up by cells far more than 15 and 30 nm particles after exposure to cells for 24 h. However, the latter’s uptake velocities are significant faster than the former before 10 h, indicating a disparity in uptake kinetics for different sized AuNPs. The finding from this study will improve our understanding in the cellular uptake mechanisms of different sized nanoparticles and have great implications in developing AuNPs-based drug carriers with various sizes for different purposes.

6.1. INTRODUCTION

Recent progress in the biomedical applications of nanotechnology has demonstrated that the intracellular uptake efficiency or kinetics of nanoparticles is greatly affected by many factors, including some intrinsic properties of particles itself, such as size,^{67, 78, 112-115} shape,^{71, 80, 112, 116} surface coating,^{67, 73, 115} sedimentation⁶⁸ and aggregation⁶⁹ effect as well as some features from the side of biological systems, for instance cell species,⁸¹ cell cycle period⁷⁷ etc. Among all of these factors, particle size has been proved as one of the most predominant features affecting cellular uptake mechanism, kinetics and other bio-reactivity *in*

vivo or *in vitro* proved by numerous groups in nanotechnology society during last few decades.^{71, 78, 117}

Despite remarkable advances made in this field, however, a critical debate in respect of the optimum particle size for internalization into cells with the maximum efficiency is still open. The data reported previously always conflicts due to lack of a unified and standard approach to image and quantify particles in the cellular uptake process so far. Further, the experimental conditions including particle materials, surface stabilizers, exposure time, cell living status and cell species often alter among different research groups, leading to inconsistent results. Any novel findings for a certain type of nanoparticles, announced breakthrough in this aspect by one research group however, might be irrelevant for another group even if the experimental conditions altered merely. Therefore, although it has been reported by several groups that particle with dimension at certain nanoscale or scale range, for instance diameter of 50 nm or below 120 nm was once regarded as the maximum size (size range) for nanoparticles internalization,^{52, 78, 112} these studies still suffer from variation of the experimental conditions and lack of quantitative analysis, making these conclusions conflict to each other.

In this paper, a systematical investigation of size effect on the cellular uptake of nanoparticles was performed. Gold nanoparticles (AuNPs), a kind of noble metal nanoparticles with wide applications in biomedical, clinical and pharmaceutical field,^{16-17, 19, 24, 82-83, 118} was applied as a model system since their size, shape and surface features can be easily manipulated with designer's anticipation.¹¹⁹⁻¹²⁰ Furthermore, unlike other conventional nanoparticles that need conjugation with extrinsic labeling agents which often suffer from dissociation or loss of activity with time, AuNPs possess unique intrinsic multiphoton absorption induced luminescence (MAIL), which can be distinguished from cell organelles based on the specific MAIL spectra, making AuNPs good alternatives for *in vitro* or *in vivo* cellular uptake studies.^{25-26, 121}

The main parameters of nanoparticles as well as the features of the bio-systems exposed to particles, including particles materials, shape, coating ligands, concentration unit and cell types and numbers were all unified for the purpose

of eliminating interference from the variation of experimental conditions at the most extent. By virtue of the unique optical properties of gold, a novel semi-quantitative approach was presented in this chapter based on the use of multiphoton laser scanning microscopy (MP-LSM) and UV/Vis spectroscopy for evaluation of the cellular uptake process of AuNPs. The AuNPs applied in this study were spherical with sizes below the resolution limit of the optical microscopy, ranging from 15 to 80 nm. This approach allows simultaneous acquisition of in situ images as well as quantitative data with respect to the amount of AuNPs uptaken by cells. In addition, it also provides a capability to distinguish particles entry into cells with those only adsorbed on cell membrane from 3D MP-LSM images, giving details in terms of the uptake process that cannot be achieved by other quantitative techniques applied at present, e.g. ICP-MS, ICP-AES. As revealed by the quantitative data, cellular uptake of AuNPs is size and time dependent process. Larger AuNPs (80 and 50 nm) can penetrate into cells in larger amount than the smaller ones (30 and 15 nm) in 24 h with relatively slower uptake velocity than the latter. Sedimentation of particles as a crucial relevant factor in this process cannot be ignored.

6.2. MATERIALS AND METHODS

6.2.1. NANOPARTICLE PREPARATION AND CHARACTERIZATION BY TEM

Colloidal AuNPs with diameter of 15 nm were prepared by Turkevich method which is typically used to produce monodisperse spherical gold nanoparticles with size of around 13-20 nm.¹⁰³ Briefly, 10 mg of tetrachloroaurate ($\text{HAuCl}_4 \cdot 3\text{H}_2\text{O}$, Sigma-Aldrich Chemie GmbH, Steinheim, Germany) was dissolved in 50 mL of ultrapure deionized water and heated to the boiling point. Then, one mL of a 37.34 mg/mL aqueous solution of sodium citrate ($\text{Na}_3\text{C}_6\text{H}_5\text{O}_7 \cdot 2\text{H}_2\text{O}$, Sigma-Aldrich) was introduced under vigorous stirring to reduce the Au^{3+} to Au^0 . The solution was kept boiling for 10 minutes with constant stirring. The resulting AuNPs were spherical with an average diameter of 15 nm. These particles were later on used as gold seeds for synthesis of larger AuNPs.

Because of a part of particles with unsatisfactory morphology produced in the synthesis process for AuNPs larger than 20 nm by Turkevich method, a seeding

growth method demonstrated by Brown *et al.* was introduced here to prepare 30 nm AuNPs¹⁰⁴. 1 mL of 15 nm AuNPs solution (2.9×10^{12} NPs/mL) was diluted with ultrapure deionized water to a volume of 40 mL as gold seeds. Then, 1.77 mL of a freshly prepared 1 mg/mL aqueous solution of tetrachloroaurate was introduced while stirring. After 1 min, 0.306 μ L hydroxylamine (NH_2OH , 50%, solution in water, Sigma-Aldrich) was quickly added to reduce the Au^{3+} . Stirring continued for 10 minutes after the color turned reddish brown. Particles prepared by this method were spherical with an average diameter of 30nm. The water used in all experiments was prepared in a Millipore Milli-Q purification system (resistivity higher than $18.0 \text{ M}\Omega \text{ cm}^{-1}$). Because some non-spherical and polydisperse particles produced as by-products on the second or third growth step, we purchased two batch of citric ligands coated AuNPs with size of 50nm and 80nm respectively, from Ted Pella Inc (Redding, California, USA).

The gold core morphology and mean diameters of the four kinds of AuNPs were determined by TEM as described in chapter 4.

6.2.2. NANOPARTICLE QUANTIFICATION BY UV/VIS SPECTROSCOPY

UV/Vis spectroscopy was carried out to determine AuNP concentration. Absorption spectra of AuNPs were recorded using a PerkinElmer diode array UV/Vis spectrophotometer (PerkinElmer, Lambda35, Netherlands). The spectra were collected using quartz cuvettes with 1 cm optical path length. The precise concentration (number concentration) of each batch of gold nanodispersion can be obtained by the following equation:¹²²

$$N = \frac{A_{450} \times 10^{14}}{d^2 \left[-0.295 + 1.36 \exp \left(- \left(\frac{d - 96.8}{78.2} \right)^2 \right) \right]} \quad (6.1)$$

where N is the number concentration of AuNPs in nps/mL (number of particles/mL), A_{450} is the absorption at 450 nm, and d is the diameter of AuNPs.

6.2.3. CELL CULTURE CONDITIONS

Human alveolar basal epithelial cells (A549 cells, CCL-185; ATCC, Manassas, VA, USA) were cultured in a 75 cm^2 flask in RPMI1640 high glucose medium

supplemented with 10% heat inactivated fetal bovine serum without phenol red (PAA Laboratories GmbH, Pasching, Austria) at 37°C under 5% CO₂. Medium was changed every second day and subculture of the cells was performed when 80% confluence was reached.

6.2.4. NANOPARTICLE UPTAKE

Evaluation of the cellular uptake extent of various sized AuNPs was performed by multiphoton laser scanning microscopy techniques to detect the intrinsic MAIL signal from gold particles entrapped by cells.

A549 cells were seeded into a 24-well plate (PAA Laboratories GmbH, Pasching, Austria) with density of 2×10^4 cells per well and grown until 90% confluence. Prior to exposure to gold particles, medium at each cell culture well was aspirated. Cells were washed with fresh medium three times before 0.5 mL of gold suspension in RPMI solution plus 10% serum without phenol red was added. All samples were then incubated at 37°C under 5% CO₂ for 24 h. The number concentration for different size AuNPs were all equalized to a value of 7.5×10^{10} particles/mL which was feasible for both small and large particles.

At 24 h, gold suspension incubated with cells was removed from each well. Cells were washed three times with PBS to remove excess AuNPs, fixed with 1% formalin and then washed an additional three times with PBS. Afterwards, 0.5 mL of a 1% Vybrant DiI cell-labeling solution (Invitrogen, Eugene, OR, USA), a lipophilic membrane dye, was added to each well and incubated for 5 minutes at room temperature. Following DiI incubation, cells were washed three times with PBS and immersed in 0.5 mL PBS solution for visualization by multiphoton laser scanning microscopy.

6.2.5. CELLULAR UPTAKE DYNAMIC OF AUNPS

Experiments for exploring the cellular uptake dynamic of AuNPs were carried out by combining MP-LSM and UV/Vis spectroscopy.

A549 cells were seeded into a 24-well plate with density of 2×10^4 cells per well and grown until 90% confluence. Immediately before co-incubation with AuNPs, medium at each cell culture well was aspirated. Cells were washed with fresh medium three times and afterwards the medium was aspirated again. 0.5 mL of

gold suspension in RPMI solution plus 10% serum without phenol red with concentration of 5.8×10^{11} , 1.36×10^{11} , 3.0×10^{10} , 4.4×10^9 particles per mL for 15, 30, 50 and 80 nm respectively, was added into each well and incubated with cells at 37°C under 5% CO₂ for defined time intervals: 1, 2, 4, 6, 8, 10, 12 and 24 hours. The number concentration of each sized AuNPs was precisely set in a suitable range in which the UV/Vis absorption of gold colloid shows good linear relationship as a function of the particles concentration. Several positive controls (no cell presence) as well as a negative control (no particles presence) were set as reference groups incubated in the same condition.

At each time point (1, 2, 4, 6, 8, 10, 12 and 24 h), the supernatant colloid AuNPs were collected from each well. Then the cells were gently washed twice using 200 µL fresh cell culture medium to get rid of excess AuNPs. Afterwards, the supernatant together with the washing medium was transferred into a clean cuvette for UV/Vis measurement. The cells were further washed with PBS once and fixed with 1% formalin and then washed an additional three times with PBS. Afterwards, 0.5 mL of a 1% DiI solution was added for each well and incubated for 10 minutes at room temperature. Following DiI incubation, cells were washed three times with PBS and immersed in 0.5 mL PBS solution for imaging by multiphoton laser scanning microscopy.

6.2.6. CONFOCAL IMAGING AND PSF DETERMINATION

The samples prepared above were visualized by an inverted confocal/multiphoton laser scanning microscopy (Zeiss LSM510 META system, Carl Zeiss, Jena, Germany) adapted with a pulsed infrared laser ($\lambda=705-980$ nm, Chameleon XR, Coherent, Germany) for multiphoton excitation. Samples were excited with 778 nm (red), 543 nm (green) laser lines. Images were captured with a 63×/1.2 NA water immersion objective lens in multi-tracking mode at an acquisition resolution of 512×512. Z-stacks of the cell samples were acquired at 0.8 µm intervals. Image stacks were analyzed using ImageJ software (<http://rsb.info.nih.gov/ij/download.html>) at a per pixel basis.

Quantification of the number of AuNPs entrapped by cells throughout each image stack was carried out using the 'analyze particles' function of the ImageJ software package, which permits visualization of either spherical or irregular

shaped objects throughout an image stack or a set of stacks and designates a spatial position along x, y and z directions together with the intensity of the spot it represents. Prior to intensity and spot area measurements, only the tracks of AuNPs were selected. The threshold was optimized to a proper value of 25 in which the background signals were eliminated completely and only AuNPs can be visualized. A summary of the number of the objects as well as total area of the optical spots was provided by the software afterwards.

Colocalization of AuNPs in cell membrane was evaluated by analyzing a set of multi-channel image stacks on a per cell level. Particles colocalized in the cell membrane (green color area) and cytoplasm was analyzed respectively. Thus the proportion of particles in the cell membrane for each cell can be determined.

The resolving power of MP-LSM used in this study can be theoretically calculated by the following equations based on Rayleigh criterion:¹²³

$$r_{xy} = \frac{0.7\lambda}{NA} \quad (6.2)$$

$$r_z = \frac{2.3\lambda n}{NA^2} \quad (6.3)$$

where, λ is the wavelength of the emitted light, NA is numerical aperture of the objective lens and n is the refractive index of the medium. The value of r_{xy} and r_z here can be calculated by using proper values for equations 6.2 and 6.3, thus the lateral (r_{xy}) and axial (r_z) resolution of the current microscope can be determined.

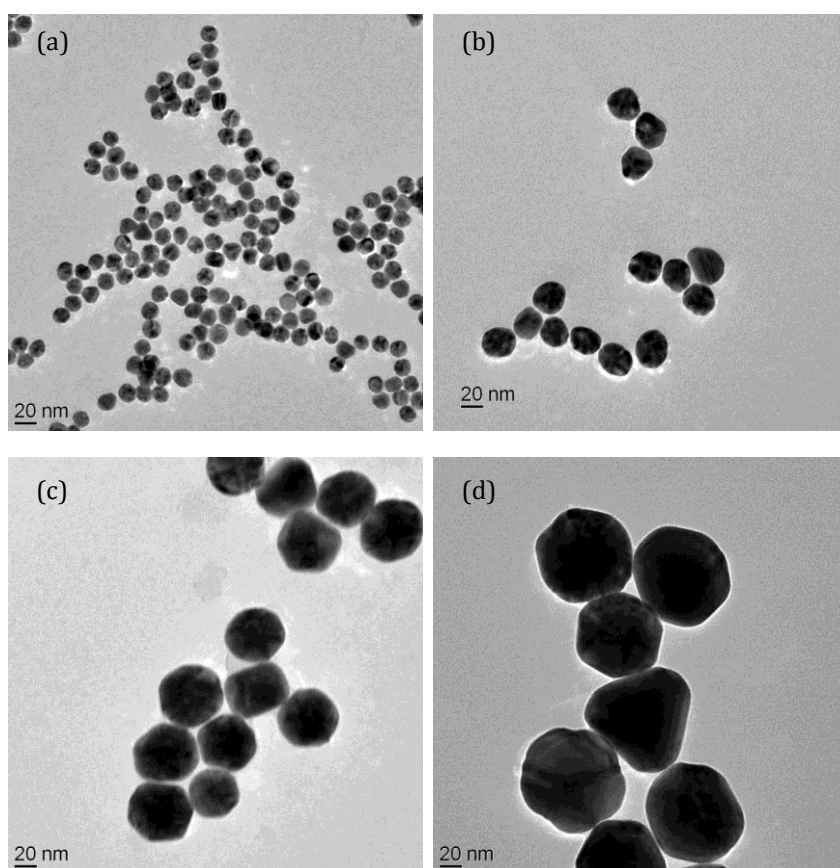
6.3. RESULTS AND DISCUSSION

6.3.1. AUNPS MORPHOLOGY

Representative TEM images (Figure 6.1a-d) illustrate that those four kinds of AuNPs are all of spherical shape and monodisperse. The average diameter of the gold core with a standard deviation as well as the zeta potential for each type of gold colloid is shown at the first two columns of Tab. 6.1.

Unlike bulk gold, gold nanospheres have distinctive optical properties. These features are determined by the interaction of conduction band electrons in the

surface atoms of AuNPs with the electric field vector of the incident light in a certain range of frequency. The incident light can induce the so-called localized surface plasmon resonance (LSPR), which occurs in the visible and near-infrared region, depending on size and shape of AuNPs. Only when the excitation wavelength is optimal to satisfy the LSPR, a distinct extinction is observed from the particles. Thus for a certain sized AuNPs, a characteristic absorption spectrum that has a distinct maximum absorption peak can be observed, shifting from 518 to 547 nm in wavelength with the increase of particles size from 15 to 80 nm (Figure 6.1e). These features can be characterized conveniently by UV/Vis spectroscopy and further exploited to measure their individual concentrations in solution by use of equation 6.1. The main parameters of their UV/Vis absorption spectra (λ_{\max} and A_{\max}) and corresponding concentrations are shown in the last three columns of Table 6.1.



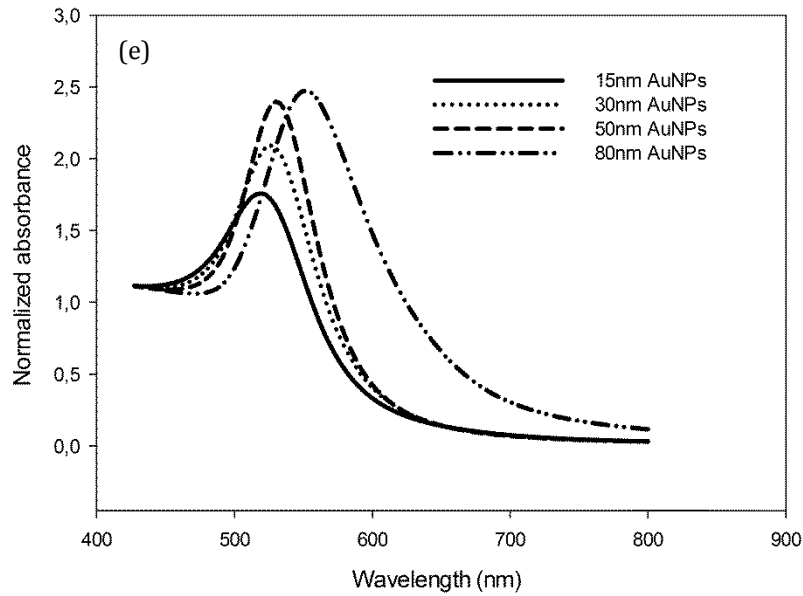


Figure 6.1. (a-d) Representative transmission electron micrographs of spherical AuNPs with diameters of 15, 30, 50 and 80 nm with their corresponding (e) normalized UV/Vis absorption spectra.

Table 6.1. Selected AuNPs characteristics

Size rang (nm)	Size of gold core (nm) ^a	Zeta potential (mV)	λ_{\max} (nm)	A_{\max}	Conc.(number of NPs/mL) ^b
15	15.59±0.77	-28.8	518	1.7418	2.9×10^{12}
30	31.43±1.34	-28.5	526	0.5354	1.01×10^{11}
50	51.98±2.58	-26.4	530	1.2207	4.5×10^{10}
80	82.29±3.12	-39.1	547	1.16	1.1×10^{10}

Note: ^a Average diameter of gold core and standard deviation of each sized AuNPs are determined by TEM measurement. ^b Concentration of AuNPs are calculated by equation 6.1.

6.3.2. SINGLE PARTICLE TRACKING OF SUBRESOLUTION AUNPS AND THRESHOLD SETTING

Due to the resolution limitation of optical techniques, a sub-resolution object exhibits an ‘optical size’ in the image instead of its real physical size. This phenomenon can be described by the point spread function (PSF). The theoretical PSF of current MP-LSM can be obtained by inputting relevant parameters into equation 6.2 and 6.3. The lateral and axial resolutions were calculated to be 320nm and 1020nm respectively. Because AuNPs used in this study (15-80 nm) are all in sizes below the optical limit, their real physical size cannot be resolved by the microscope. However, from diffraction theory, we know a single subresolution particle in a MP-LSM is presented like a particle with radius of around 320nm. Based on this principle, an optical spot of the image with an area of $0.322 \mu\text{m}^2$ ($0.32 \mu\text{m} \times 0.32 \mu\text{m} \times 3.14$) can be regarded as

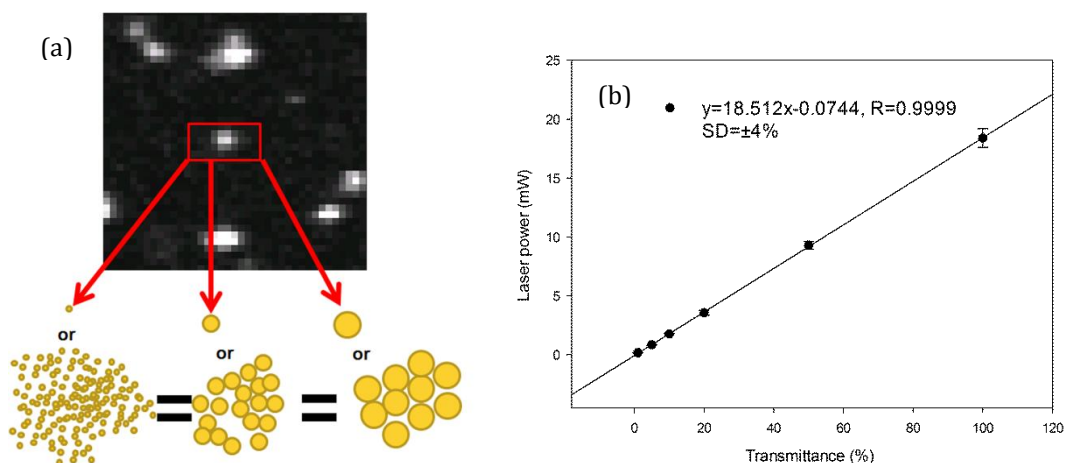
the minimum resolvable 'spot unit' representing one or more sub-resolution AuNP not exceeding its spot size.

Since there is still very high possibility for one spot unit containing a number of AuNPs, investigation on the signal intensity distribution of different sized AuNPs is necessary. For instance, theoretically one spot unit might contain 15, 50 or 80 nm AuNPs with a total number from at least 1 to at most 1819, 163 or 64 respectively illustrated as Figure 6.2a. Obviously, with the growth of particles number assembled in one spot, the contribution to the image intensity increases as well.

The principal idea for the studies is based on the assumption that one spot unit which contains only one single AuNPs would emit minimum luminescent/SHG signal with intensity at a low threshold level, whereas the spot containing maximum number of particles emits light with intensity up to the highest threshold. Through this principle, the number of monodisperse AuNPs entrapped by cells can be estimated by counting the number of AuNPs with emission intensity within a proper threshold regime extracted from a series of 3D image stacks.

Under certain excitation conditions, the signals of small particles (15 nm, 30 nm) can be distinguished from background at the threshold of an intensity value of 25 above which the noise signals are completely subtracted. Thus, the value of 25 is set as a lower threshold for particle tracking. As a result of the fact that the multiphoton laser power is pulse energy fluctuating periodically with approximately $\pm 4\%$ variance (Figure 6.2b), the emission light induced under such laser excitation, even from same AuNPs would fluctuate within a certain range as well, instead of keeping a constant value. These intensity value ranges should allow us to identify single particle based on the emission intensity. Our study (Figure 4.7a) shows that the emission intensity of single AuNPs (15 nm, 30 nm) excited at 780 nm under the same laser power fluctuates slightly with ± 10 intensity units. Thus the threshold range for screening individual AuNPs with smaller sizes (15 nm, 30 nm) was set from 25 to 34. Likewise, the threshold range for larger particles (50 nm, 80 nm) was set from 25 to 44 because their emission intensities were 1.8 times higher than the smaller ones.

When it is known that the luminescence comes from a unit spot, the emission with intensity in the lowest threshold level (25-34) is estimated generated from a single AuNPs with size of 15 nm or 30 nm. Similarly, the correspondence threshold range for individual AuNPs with larger sizes (50 nm, 80 nm) is set as 25-44. Based on the same principle, the emission signals with intensities over those lowest levels are estimated from agglomerated AuNPs. Figure 6.2c,d shows the intensity distribution in each threshold regime of unit spot extracted from image stacks of various AuNPs (15, 30, 50 and 80 nm) exposed to A549 cells for 24 h. The data demonstrates that on average over 50% of the optical unit spots distribute in the lowest threshold range; far more than the spots in other threshold regions, indicating that the majority numbers of AuNPs still maintain a non-agglomerated state. On the other hand, the super bright unit spots (in threshold 235-255) which are estimated containing the maximum numbers of single particles accounts for very small proportion only from 0.1%-1.5%. This proves that the population of agglomerated AuNPs plays negligible role affecting the statistics on the number of AuNPs entrapped by cells. Hence, the cellular uptake extent of AuNPs can be evaluated quantitatively by analyzing the number of non-agglomerated AuNPs only, which are assumed emitting light with intensity in the lowest threshold range. This finding will greatly reduce the complexity and cost of calculation work on the evaluation process associated with vast known or unknown influencing factors.



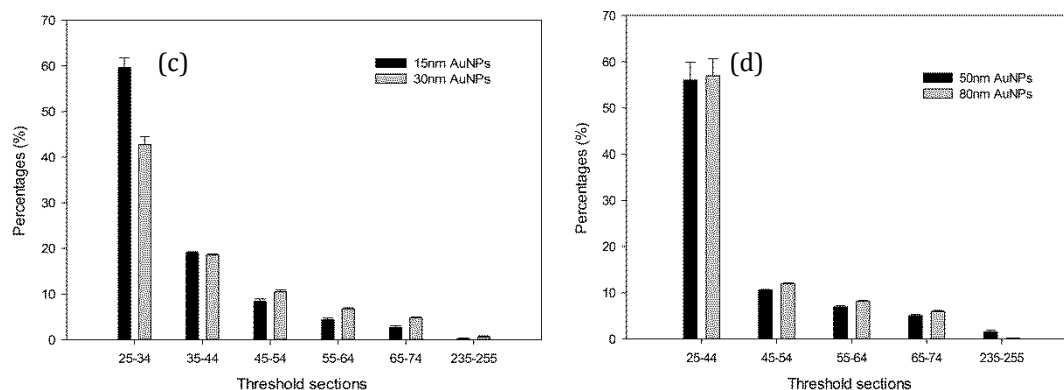


Figure 6.2. (a) Schematic illustration of an optical unit spot representing various sized AuNPs with different numbers. (b) A mean slope curve of the laser power as a function of lens transmittance. The SD value for each spot is roughly $\pm 4\%$, and intensity distribution in each threshold regime of AuNPs with size of (c) 15nm, 30nm, (d) 50nm and 80nm.

6.3.3. AUNPS CONCENTRATION UNIT SETTING

Considering some of the conflicting results caused by the use of different particle concentration unit among different research groups, selecting a suitable concentration unit of particles is a crucial issue. The most common used concentration unit is mass concentration, which is on an equal mass-dose of raw materials basis. Concerning the fact that it is the individual particles that deliver the drugs or biomolecular into the target site of cells and acts its function, being aware of particle number is more meaningful than only knowing the mass dose of raw materials prior to nanoparticles. Therefore, instead of mass concentration, number concentration was applied in our study as a standard concentration unit of AuNPs. The doses of AuNPs with different sizes were normalized to the equivalent particles number before exposure to cells. The difference between those two kinds of concentration unit is illustrated by Figure 6.3a,b.

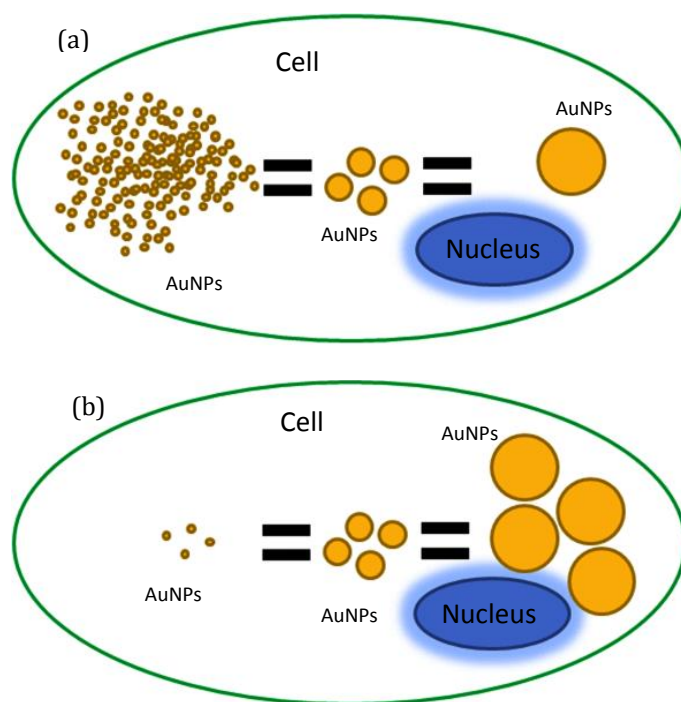


Figure 6.3. Schematic representation of the equivalent amount of various sized AuNPs engulfed by a cell based on mass concentration unit (a) and number concentration unit (b) respectively.

6.3.4. CELLULAR UPTAKE OF AuNPs

Spherical AuNPs at four representative sizes (15, 30, 50 and 80 nm) were applied in this study. The other relevant parameters including surface stabilizer, particle concentration, cell numbers and incubation time *etc.* were all set identical as mentioned previously in the method section, to avoid interference from a variation of the experimental conditions.

The cellular uptake process was monitored using MP-LSM. By counting the number of non-agglomerated particles internalized into cells from a 3D stack of MP-LSM images, cellular uptake extent of different sized AuNPs can be determined.

Figure 6.4a-d shows four representative panels derived from a z-series of MP-LSM images, illustrating AuNPs with various sizes are all able to gain intracellular access into A549 cells after 24 h exposure. AuNPs are detectable in slices at all levels from the 3-D images, suggesting their internalization in cells not only loosely adsorbed on the outer surface of cell membrane.

In Figure 6.4e, a bar graph concerning the number of monodisperse AuNPs in/on cells per optical stack versus diameter of AuNPs shows cellular uptake is

heavily dependent on the size of particles. Because it is difficult to precisely count the number of irregular shaped cells, we used the unit of AuNPs per optical stack instead of the number of particles per cell. This method allows standardization of measurements.

The uptake efficiency increases greatly with the growth of particle size and the maximum uptake occurs at a particle size of 80nm. There could be two reasons for this phenomenon. On one hand, considering the biological factors, we assume larger particles might enter cells via receptor-mediated endocytosis more efficiently than smaller ones. Besides, some non-biological factors also are also crucial and cannot be ignored. For instance, the difference in sedimentation rate between small (15, 30 nm) and larger (50, 80 nm) particles had to be taken into account. Because in a typical *in vitro* cellular uptake experiment, the nanoparticles are always assumed to be well dispersed in the cell culture medium and the concentration of particles at the cell surface is assumed to be constant. However, virtually, some larger and heavier particles can sediment more quickly than those smaller ones and therefore causing the dose of nanoparticles on the cell surface to vary, thus dramatically influencing the uptake extent. But those assumptions need to be further verified by uptake dynamic study described in the following.

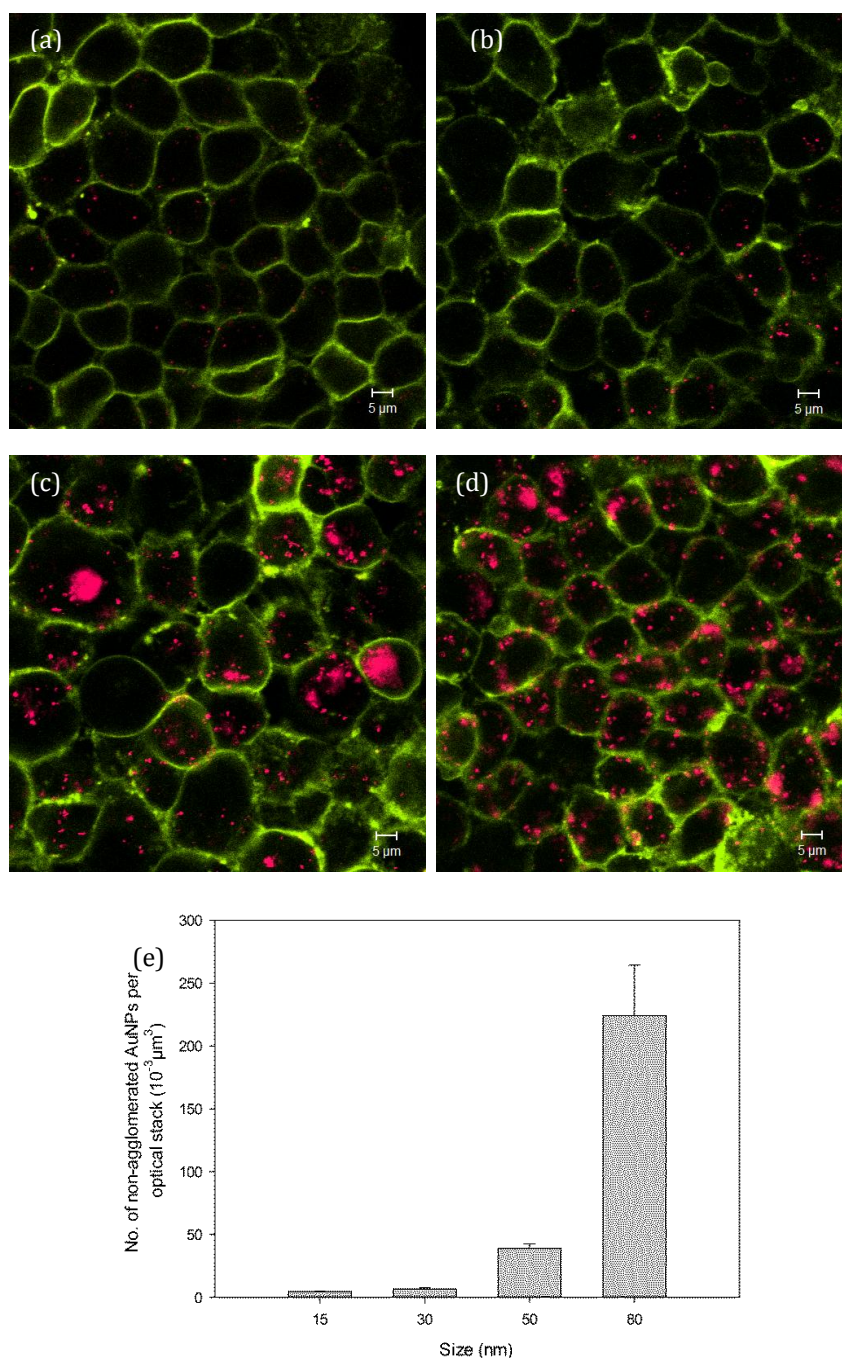


Figure 6.4. (a-d) CLSM and MP-LSM images of AuNPs with sizes of 15, 30, 50, 80 nm respectively, after incubation of A549 cells for 24 h. Green color represents cell membrane stained with DiI and red color spots represent AuNPs. Laser wavelength for excitation of AuNPs is optimized to $\lambda_{em}=778$ nm. The number concentration of various sized AuNPs exposure to A549 cells was set to 7.5×10^{10} particles/mL. (e) The bar graph depicts the amount of non-agglomerated AuNPs per optical stack vs nanoparticles size.

6.3.5. KINETICS OF PARTICLE ENTRY

We conducted the studies of cellular uptake kinetics by incubating A549 cells with various sized AuNPs for different period of time. The studies were achieved using two different approaches: 1) we count the number of non-agglomerated

AuNPs in cells through MP-LSM image analysis; in the meantime 2) we also measure the content of AuNPs maintained in cell culture medium by UV/Vis method. MP-LSM image analysis reveals that the uptake kinetics of AuNPs greatly differs with the variation of particle size. As shown in Figure 6.5a-d, the first sign of all sized AuNPs trapped by cells are observed at 1 h, but after that they exhibit different uptake degrees.

For AuNPs with size of 15 nm, the uptake slowly climbs up in the first 6 h, then significantly jumps to a high level at 8 h, after which the rate steadily increases until reaches the maximum value at 24 h. For AuNPs with size of 30 nm and 50 nm, similar trends are shown: the uptake extent increases slowly in the first 12 h before getting to the maximum point at 24 h. Differing with them, however, 80 nm AuNPs displays a nearly constant uptake degree during most of the exposure time from 1 h to 10 h. A significant increase of uptake is seen arising from 12 h to the maximum degree at 24 h which is far higher than those at other time points. This disparity in uptake kinetics for different sized AuNPs has never been reported previously and will be further explored later in this study.

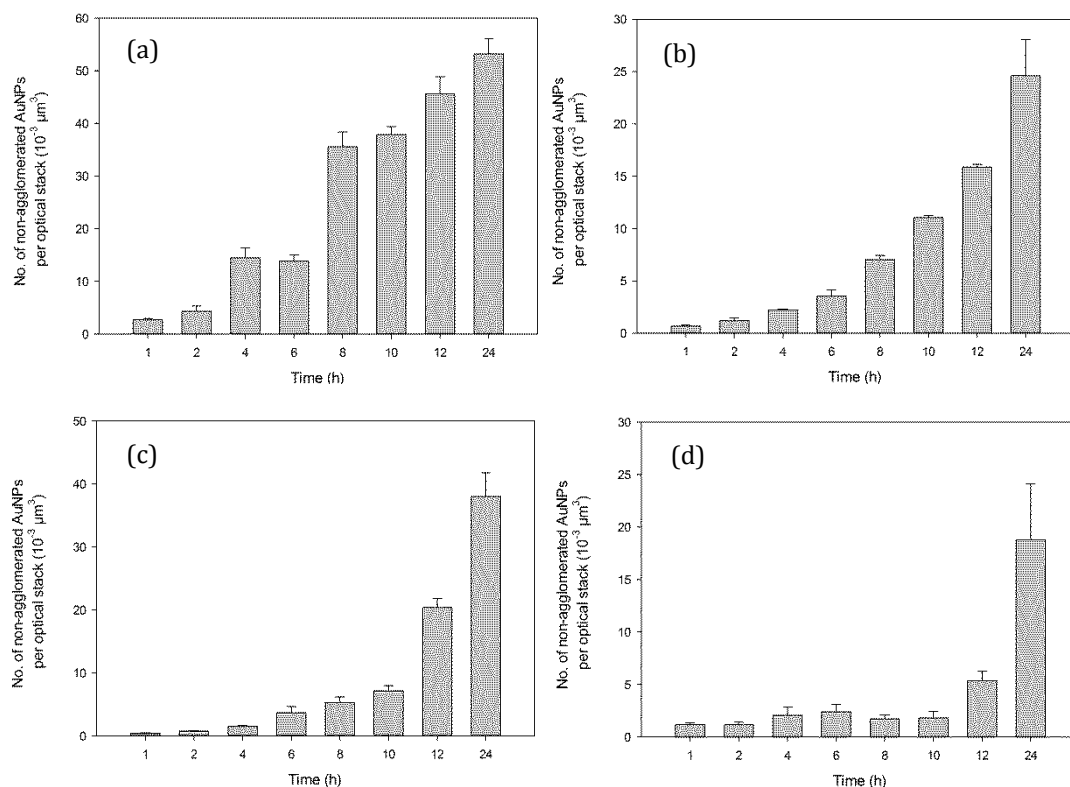


Figure 6.5. Quantitative evaluation of cellular uptake extent of AuNPs with sizes of (a) 15 nm, (b) 30 nm, (c) 50 nm and (d) 80 nm in different time point by MP-LSM analysis.

By exploiting the unique optical properties of AuNPs, UV/Vis spectroscopy as a macroscopic quantitative approach was applied here to verify whether the data obtained from MP-LSM image analysis can imply the real uptake extent of AuNPs in cells.

Based on the Beer–Lambert law, the concentration of AuNPs has a linear correlation with the absorbance of their localized surface plasmon resonance (LSPR) peak (Figure 6.6a-d).¹²⁴ Through this way, the concentration of AuNPs in cell culture medium can be directly obtained. Thus the number of AuNPs taken up by cells per well at each time point can be determined by subtracting the gold amount in the medium from the total gold dose applied.

The initial concentration for each type of AuNPs was obtained by equation 6.1. Figure 6.7a-d shows the UV/Vis spectra of the different sized AuNPs dispersed in a culture medium, before and after 1 and 24 h incubation of the cells respectively. It is clearly to see the maximum peak intensities of AuNPs decrease over time, indicating uptake of AuNPs by cells. Because the range of the best-fit linear correlation between the concentration of AuNPs and the absorption of LSPR peak differs with the change of particle size, it is hard to keep an identical initial concentration for all kinds of AuNPs. Thus, different initial concentrations for these four kinds of AuNPs were applied shown in the notation of Figure 6.7. Due to this reason, the investigation on the uptake percentage relative to the total amount of particles, instead of on its absolute value for each kind of AuNPs is more meaningful.

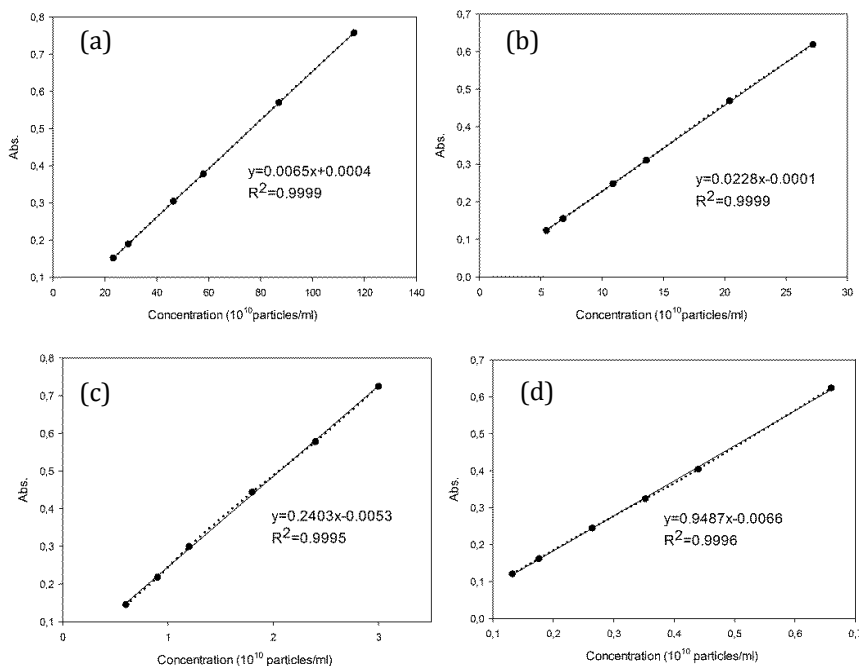


Figure 6.6. Calibration curves for the four types of AuNPs. (a) 15 nm AuNPs; (b) 30 nm AuNPs; (c) 50 nm AuNPs; and (d) 80 nm AuNPs. The calibration curves were obtained in the cell culture medium after 24 h of incubation at 37°C and 5% CO₂. N=3 for each point. The deviation was less than 1% from average values. For all the plots, the calibration curves were obtained with $R^2 > 0.99$.

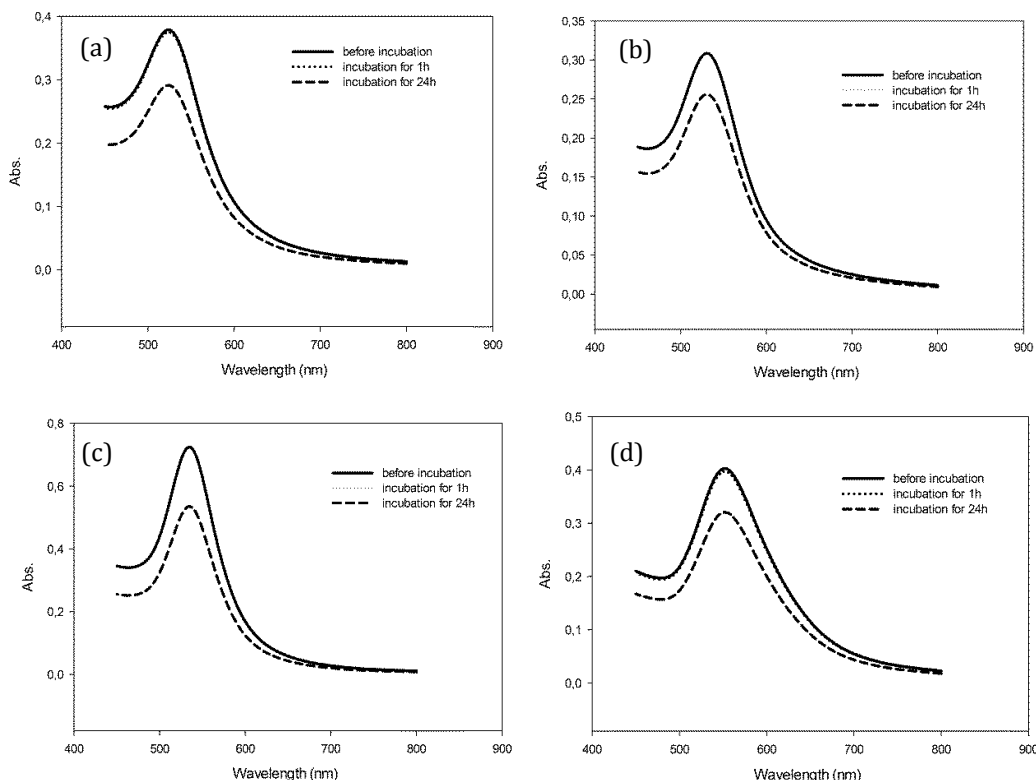


Figure 6.7. UV/Vis spectra of different sized AuNPs. The concentrations of particles (based on particle number) before incubation with the cells are: (a) 5.8×10^{11} particles/mL (15 nm AuNPs); (b) 1.36×10^{11} particles/mL (30 nm AuNPs); (c) 3.0×10^{10} particles/mL (50 nm AuNPs); (d) 4.4×10^9 particles/mL (80 nm AuNPs). After 24 h incubation with cells, the maximum peak intensities of AuNPs decreased relative to those of before incubation, indicating uptake of AuNPs by cells during incubation.

Figure 6.8 a-d summarizes the percentage of cellular uptake per well for different types of AuNPs at each time point measured by UV/Vis analysis. Significantly, the uptake percentages increase over time for all types of AuNPs, illustrating it is a time dependent process. Further, the uptake extent was also found sensitive to particle size. As the AuNPs becomes larger, their uptake processes slow down greatly. This result is consistent with previous data acquired by using MP-LSM image analysis method, confirming these two methods are highly correlated to each other and both of them can imply the in vitro cellular uptake results of AuNPs.

From these uptake graphs, there is one point being worth emphasizing that during most of the incubation time (0-12 h) the uptake extent of larger sized AuNPs (50, 80 nm) is far less than that of small ones, however, after a long time incubation (24 h) their uptake extent still reaches a high level being equivalent to that of smaller particles. To explain these different uptake behaviors for various sized AuNPs we depict a whole uptake process as following three steps: 1) AuNPs are transported from any arbitrary zone of the suspending medium to the contact zone (Figure 6.9) and 2) adsorbed on the surface of cell membrane, then 3) penetrate into cells through protein-mediated or any other receptor-mediated pathway.

Obviously the uptake only occurs after AuNPs are transported to contact zone. Therefore, the concentration of particles in contact zone can be assumed as a critical factor for cellular uptake process.

As shown in Figure 6.9, AuNPs can be transported to contact zone through diffusion and sedimentation. Considering the sedimentation effect is caused by gravitational forces that highly depend on particles mass which are proportional to the cube of particles radius, it is imperative to investigate the sedimentation effect for different sized AuNPs.

Figure 6.10 gives a comparison of sedimentation effect for four types of gold dispersion over a period of 48 h, exhibiting a clear disparity in sedimentation effect for these particles. For AuNPs with size of 15 and 30 nm, their concentrations keep nearly constant relative to the initial concentration even after 48 h. In contrast, for particles with sizes of 50 and 80 nm, significant

declining trends of particle concentration are seen particularly after a long period, for instance, 24 h and 48 h. We note that after 24 h incubation almost 7% and 12% of gold concentration lose due to sedimentation effect for 50 and 80 nm AuNPs respectively, revealing that it is sedimentation that contributes to the high penetration extent for bigger sized AuNPs at 24 h. This result also very well explains the abnormal uptake rate of these two types of AuNPs at 24 h observed previously in Figure 6.5 and Figure 6.8.

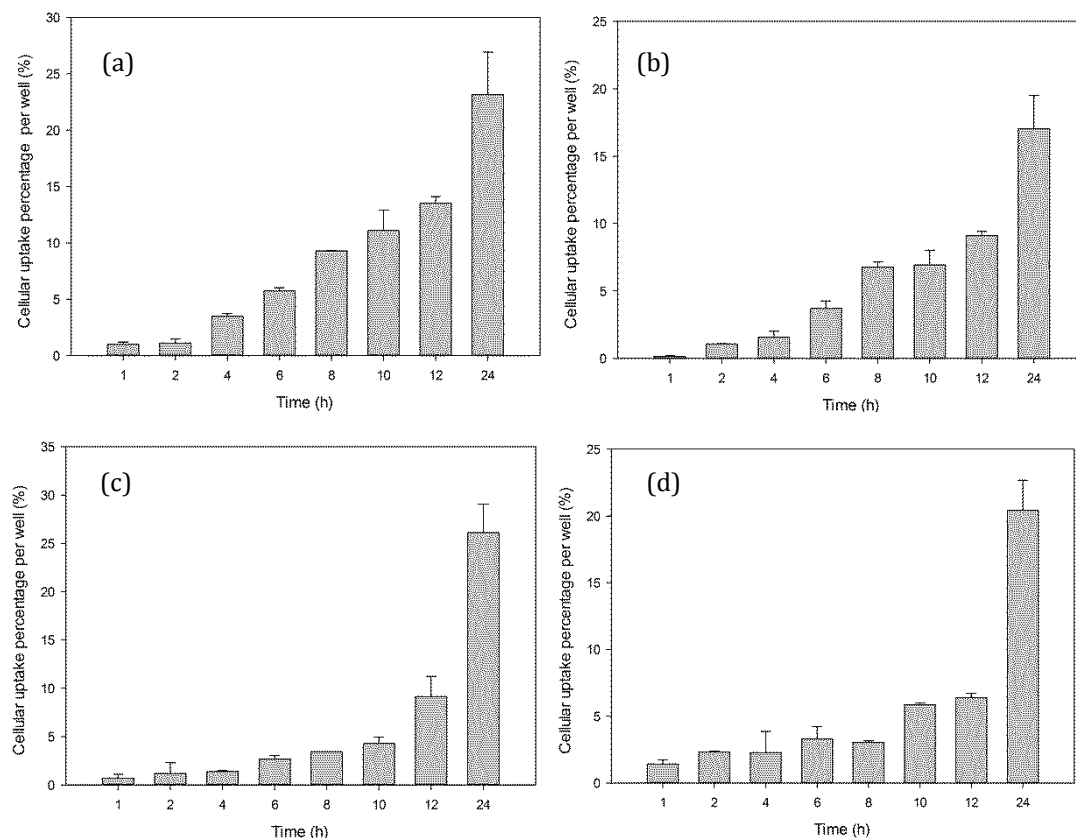


Figure 6.8. Quantification of the uptake percentage of AuNPs into cells relative to the total amount of particles applied per well at different time point by UV/Vis analysis. The initial gold amounts applied per cell growth well are: (a) 2.9×10^{11} particles (15 nm AuNPs); (b) 6.8×10^{10} particles (30 nm AuNPs); (c) 1.5×10^{10} particles (50 nm AuNPs) and (d) 2.2×10^9 particles (80 nm AuNPs). A549 cells were incubated with different sized AuNPs at 37°C with defined concentration mentioned above and at each time point the suspension medium were collected and analyzed for gold concentration by UV/Vis.

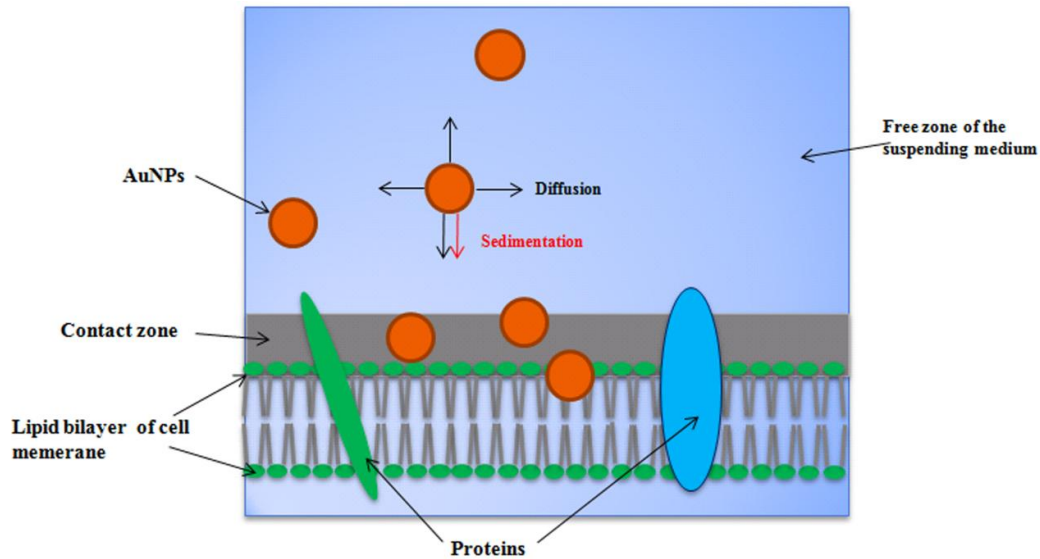


Figure 6.9. Representation of the cellular uptake process of colloidal gold. The uptake extent is determined by particles concentration in contact zone which highly depends on the sedimentation and diffusion velocity of AuNPs.

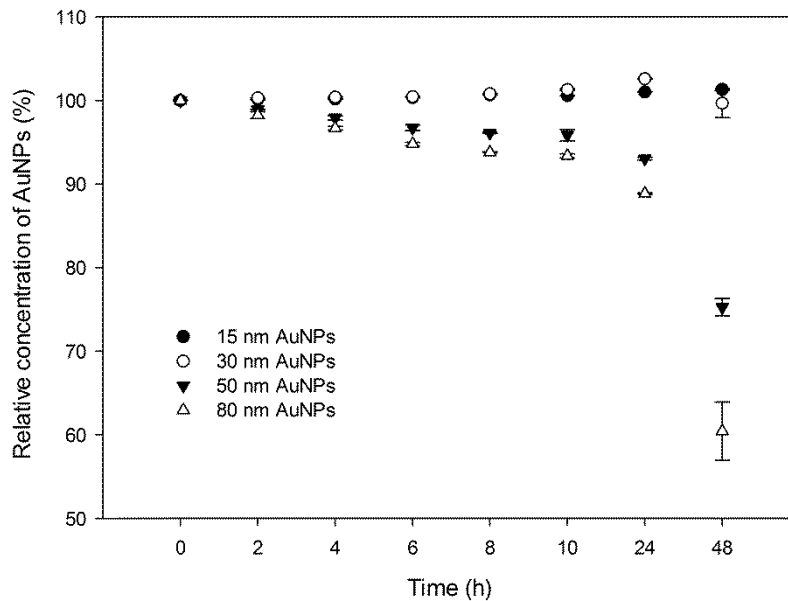


Figure 6.10. Sedimentation effects of 15, 30, 50 and 80 nm AuNPs at a series of time points from 0 h to 48 h in cell grow medium.

6.3.6. CELL MEMBRANE PENETRATION ABILITY OF AUNPS

It is well known that the cell membrane is the major barrier for cells protecting against foreign invaders also preventing the entry of particles. Hence, investigating the membrane crossing ability for different sized particles might be helpful for explaining their difference in cellular uptake kinetics. AuNPs with sizes of 15 and 80 nm were selected in this study because of their significant

difference in uptake dynamics. Particles were visualized and quantified by MP-LSM analysis at a single cell level.

Figure 6.11a shows a panel of typical 3-D MP-LSM images in orthogonal mode, exhibiting a view of the distribution of 80 nm AuNPs in one cell following 24 h incubation. The cross section image (left bottom) along with its two corresponding longitudinal section images (left top and right bottom) was displayed. Due to the cell membrane staining, AuNPs embedded in cell membrane (marked with blue arrows) and cytoplasm (marked with white arrows) can be easily differentiated, enabling us to precisely quantify the number of AuNPs localized in them separately.

Figure 6.11b shows the proportions of the particles (15, 80 nm) localized in cell membrane relative to in entire cells that change in the period of incubation time. 15 nm AuNPs exhibits a moderate declining trend from 40% at 1 h down to 22% at 24 h. In contrast, 80 nm AuNPs also display a declining trend but with a steep slope. The majority of particles (70-80%) are observed localized in the cell membrane instead of in the cytoplasm in the first 6 h. Even after 12 h, AuNPs still undergo the block from this barrier confirmed by the appearance of around 40% particles in the membrane. After 24 h, however, their proportions are found deeply reduced to 16% even below the level of 15 nm particles.

These observations can be explained with two aspects: 1) small particles (15 nm) own preferable membrane crossing ability relative to their 80 nm counterparts, for this reason we found far higher portion of 80 nm AuNPs locked in cell membrane than 15 nm ones in the first 12 h of exposure; however 2) with the incubation time going on, more and more 80 nm AuNPs sediment, leading to higher dose of these particles presented in the 'contact zone' over the cell membrane (Figure 6.9) and therefore dramatically increasing their uptake degree. This explanation are well confirmed by their high uptake percentages at 24 h expressed in Figure 6.5, Figure 6.8 and further supported by the sedimentation data in Figure 6.10. These results also give a clear answer to our assumption in respect of the uptake efficiency for different sized AuNPs mentioned in last section, that it is sedimentation effect rather than any other factors that lead the highest uptake extent for bigger sized AuNPs (50, 80 nm).

However, within a short period of exposure small particles show advantages in uptake efficiency over their big sized counterparts. To our knowledge, these results have never been reported previously and will contribute to advance understanding of the cellular uptake mechanism of nanoparticles with different sizes.

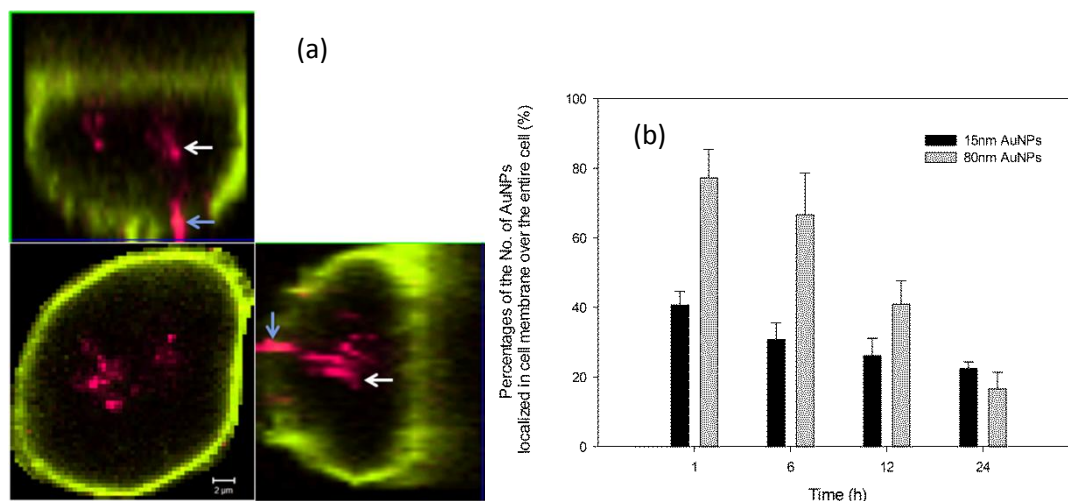


Figure 6.11. (a) A stack of representative 3D images of 80 nm AuNPs embedded into one A549 cell after 24 h incubation. A cross section view (left bottom) and its two corresponding longitudinal section views (left top and right bottom) are displayed. (b) A comparison of the proportion of particles localized in cell membrane relative to the total cell during different period of incubation time.

6.4. CONCLUSIONS

In conclusion, for the first time, a combined MP-LSM image-UV/Vis spectroscopic analysis method was applied in this paper for systematically investigating the size effect on cellular uptake process of AuNPs. Our study demonstrated different cellular uptake degrees and kinetics for a series of AuNPs with different sizes.

50 and 80 nm AuNPs sediment faster than the smaller ones (15 and 30 nm), dramatically increasing the number of particles gathered in the 'contact zone' after 24 h exposure of A549 cells, thus leading to their uptake extent with higher levels than the latter. However, in a short period of incubation time within which the sedimentation effect is negligible (10 h), small particles exhibit superior penetration ability over their bigger sized counterparts.

Our data reveals that size effect plays a great role in the cellular uptake behavior of nanoparticles and the penetration kinetics decline dramatically with the

increase of particle size. The internalization of various sized AuNPs was found continuously increasing over time with specific rates which were highly dependent on particles' sizes. And no saturation of uptake was found during 24 h demonstrating an additional uptake potential of AuNPs in A549 cells. Moreover, the data also suggest the sedimentation of particles and incubation time are two crucial and high relevant factors that need to be taken into account as one plan to conduct a cellular uptake experiment of nanoparticles with various sizes, particularly with those large and heavy particles. Considering all studies on this aspect so far, still have been performed with an empirical incubation time by arbitrary setting without considering the sedimentation effect, our study might give important inspiration and guidance to those who plan future studies to avoid erroneous and misleading results.

Overall, our studies are expected to help researchers/scientists for a better understanding of the mechanism and kinetics behind the cellular uptake process of different sized particles, allowing pharmaceutical scientists to optimize more efficient drug or gene nanocarriers by tuning their size for diagnostic and therapeutic applications.

7. SUMMARY

Cellular uptake behavior of nanoparticles along with their relevant influencing factors has been of great interest for design of nanoparticles-based DDS. With all the knowledge so far collected on this aspect, however, there are still no definite answers in terms of the effect of many crucial physic-chemical properties of particles including size, shape, surface materials and charge *etc*, on the cellular uptake sequence of particles due to extensive variations in the experimental conditions. A unified approach for imaging and quantification is still lacking.

In this study we focused on the detection of the entry of nanoparticles (with particular emphasis on gold) into A549 cells. We studied the effect of particles size on the cellular uptake efficiency and dynamics in A549 cells, using AuNPs with defined size range (15-80 nm) through a combined “multiphoton imaging-UV/Vis spectroscopic analysis” method for simultaneous imaging and quantification.

In the first section of this thesis we have systematically investigated the MAIL properties of AuNPs in a wide range of sizes (10-80 nm). The MAIL of gold was verified to be a two photon absorption induced process. For short wavelengths the signal is a combination of luminescence and SHG, being responsible for the ease of visualization of AuNPs. By taking advantage of this intrinsic optical property, AuNPs in a wide size range (10-80 nm) can be clearly visualized without need for additional fluorophores. The highest emission S/N ratio can be obtained under excitation with wavelengths between 780 nm and 840 nm. Remarkable light scattering signals involving SHG were induced from AuNPs under multiphoton excitation in a broad wavelength range (710-860 nm) with intensities overwhelming the MAIL. The optimum excitation wavelength for discrimination of AuNPs is 900 nm, upon which fingerprint-like MAIL spectrum can be easily detected without interference from SHG. This emission spectrum shows high stability and specificity, in spite of the variation of excitation wavelengths and the type of microscope used.

As the second section of this work, the MAIL profiles of AuNPs exposed to complex physical (with presence of other semiconductor nanoparticles) or/and

biological surrounding environments (living cell, human skin) were studied. The fingerprint-like MAIL spectrum of AuNPs allows easy visualization and discrimination of gold in contact with complex background, making MAIL a powerful intrinsic luminescent probe for imaging and identifying single AuNPs in cellular compartments and organelles.

In the third section of this thesis a comprehensive quantitative study on the cellular uptake sequence of different sized AuNPs (15-80 nm) in A549 cells were performed by using a combined “multiphoton imaging-UV/Vis spectroscopic analysis” method, which allows simultaneous visualization and quantification of the entry of particles into cells. 80 nm and 50 nm AuNPs were found to be taken up by cells far more than 30 nm and 15 nm particles after exposure to cells for 24 h. However, the latter’s uptake velocity was significant faster than the former in 10 h, before which the sedimentation effect of bigger sized AuNPs occurs slightly. This sedimentation effect of particles over time can be precisely evaluated by UV/Vis spectroscopic analysis. Further, this technique provides a capability for differentiating AuNPs colocalized in external or/and internal subcellular components e.g. cell membrane and cytoplasm respectively. Data exhibits higher cell membrane crossing rate of 15 nm AuNPs rather than 80 nm AuNPs in 12 h. These results reveal that when investigating the cellular uptake capability of nanoparticles in a large range of sizes, sedimentation effect of those larger and heavier particles has to be taken into account in any cases.

In summary, we have systemically studied the cellular uptake process of various sized AuNPs in A549 cells. Based on the unique MAIL properties of colloidal gold and corresponding LSPR, a novel “multiphoton imaging-UV/Vis spectroscopic analysis” approach was developed. This technique permits the wide-field visualization of single nanoparticles in cellular compartments through PSF analysis, as well as quantification on the number of AuNPs colocalized in different cell organelles, thereby providing precise and reliable quantitative information in terms of the number of particles uptaken by cells at a high throughput level. From a practical point of view, moderate measurement conditions which do less harm to samples and short data acquisition time making this technique a remarkable alternative over those currently used

approach for imaging or quantification of gold e.g. TEM and ICP-AES. By owning these advantages this method is hopefully to be developed as a standard imaging and quantification approach utilized in cellular uptake study to address many aspects of the impacts on the cellular uptake of either luminescent metallic nanoparticles or other fluorescent nanoparticles.

8. BIBLIOGRAPHY

- [1] Kreuter, J. (2007) Nanoparticles--a historical perspective, *Int J Pharm* 331, 1-10.
- [2] Allen, T. M., and Cullis, P. R. (2004) Drug delivery systems: entering the mainstream, *Science* 303, 1818-1822.
- [3] Bangham, A. D., Standish, M. M., and Watkins, J. C. (1965) Diffusion of univalent ions across the lamellae of swollen phospholipids, *J Mol Biol* 13, 238-252.
- [4] Gregoriadis, G. (1976) The carrier potential of liposomes in biology and medicine (first of two parts), *N Engl J Med* 295, 704-710.
- [5] Gelperina, S., Kisich, K., Iseman, M. D., and Heifets, L. (2005) The potential advantages of nanoparticle drug delivery systems in chemotherapy of tuberculosis, *Am J Respir Crit Care Med* 172, 1487-1490.
- [6] Hutter, E., and Maysinger, D. (2011) Gold nanoparticles and quantum dots for bioimaging, *Microsc Res Tech* 74, 592-604.
- [7] Li, W., and Szoka, F. C., Jr. (2007) Lipid-based nanoparticles for nucleic acid delivery, *Pharm Res* 24, 438-449.
- [8] Puri, A., Loomis, K., Smith, B., Lee, J. H., Yavlovich, A., Heldman, E., and Blumenthal, R. (2009) Lipid-based nanoparticles as pharmaceutical drug carriers: from concepts to clinic, *Crit Rev Ther Drug Carrier Syst* 26, 523-580.
- [9] Hillaireau, H., Le Doan, T., and Couvreur, P. (2006) Polymer-based nanoparticles for the delivery of nucleoside analogues, *J Nanosci Nanotechnol* 6, 2608-2617.
- [10] Martinez, A., Benito-Miguel, M., Iglesias, I., Teijon, J. M., and Blanco, M. D. (2012) Tamoxifen-loaded thiolated alginate-albumin nanoparticles as antitumoral drug delivery systems, *J Biomed Mater Res A* 100, 1467-1476.
- [11] Elzoghby, A. O., Samy, W. M., and Elgindy, N. A. (2012) Albumin-based nanoparticles as potential controlled release drug delivery systems, *J Control Release* 157, 168-182.
- [12] Abbasi, S., Paul, A., Shao, W., and Prakash, S. (2012) Cationic albumin nanoparticles for enhanced drug delivery to treat breast cancer: preparation and in vitro assessment, *J Drug Deliv* 2012, 686108.
- [13] Sebak, S., Mirzaei, M., Malhotra, M., Kulamarva, A., and Prakash, S. (2010) Human serum albumin nanoparticles as an efficient noscapine drug delivery system for potential use in breast cancer: preparation and in vitro analysis, *Int J Nanomedicine* 5, 525-532.
- [14] Labouta, H. I., and Schneider, M. (2010) Tailor-made biofunctionalized nanoparticles using layer-by-layer technology, *Int J Pharmaceut* 395, 236-242.
- [15] Reum, N., Fink-Straube, C., Klein, T., Hartmann, R. W., Lehr, C. M., and Schneider, M. (2010) Multilayer coating of gold nanoparticles with drug-polymer coadsorbates, *Langmuir* 26, 16901-16908.
- [16] Pissuwan, D., Niidome, T., and Cortie, M. B. (2011) The forthcoming applications of gold nanoparticles in drug and gene delivery systems, *J Control Release* 149, 65-71.
- [17] Mandal, S., Bakeine, G. J., Krol, S., Ferrari, C., Clerici, A. M., Zonta, C., Cansolino, L., Ballarini, F., Bortolussi, S., Stella, S., Protti, N., Bruschi, P., and Altieri, S. (2011) Design, development and characterization of multi-functionalized gold nanoparticles for biodetection and targeted boron delivery in BNCT applications, *Appl Radiat Isot.*
- [18] Brown, S. D., Nativo, P., Smith, J. A., Stirling, D., Edwards, P. R., Venugopal, B., Flint, D. J., Plumb, J. A., Graham, D., and Wheate, N. J. (2010) Gold nanoparticles for the improved anticancer drug delivery of the active component of oxaliplatin, *J Am Chem Soc* 132, 4678-4684.

- [19] Ghosh, P., Han, G., De, M., Kim, C. K., and Rotello, V. M. (2008) Gold nanoparticles in delivery applications, *Adv Drug Deliv Rev* 60, 1307-1315.
- [20] Walkey, C., Sykes, E. A., and Chan, W. C. (2009) Application of semiconductor and metal nanostructures in biology and medicine, *Hematology Am Soc Hematol Educ Program*, 701-707.
- [21] Seow, W. Y., Xue, J. M., and Yang, Y. Y. (2007) Targeted and intracellular delivery of paclitaxel using multi-functional polymeric micelles, *Biomaterials* 28, 1730-1740.
- [22] Aryal, S., Pilla, S., and Gong, S. (2009) Multifunctional nano-micelles formed by amphiphilic gold-polycaprolactone-methoxy poly(ethylene glycol) (Au-PCL-MPEG) nanoparticles for potential drug delivery applications, *J Nanosci Nanotechnol* 9, 5701-5708.
- [23] van Vlerken, L. E., and Amiji, M. M. (2006) Multi-functional polymeric nanoparticles for tumour-targeted drug delivery, *Expert Opin Drug Deliv* 3, 205-216.
- [24] Schneider, M., Reum, N., Fink-Straube, C., Klein, T., Hartmann, R. W., and Lehr, C. M. (2010) Multilayer Coating of Gold Nanoparticles with Drug-Polymer Coadsorbates, *Langmuir* 26, 16901-16908.
- [25] Polavarapu, L., Manna, M., and Xu, Q. H. (2011) Biocompatible glutathione capped gold clusters as one- and two-photon excitation fluorescence contrast agents for live cells imaging, *Nanoscale* 3, 429-434.
- [26] Kneipp, J., Kneipp, H., McLaughlin, M., Brown, D., and Kneipp, K. (2006) In vivo molecular probing of cellular compartments with gold nanoparticles and nanoaggregates, *Nano Lett* 6, 2225-2231.
- [27] Le Guevel, X., Trouillet, V., Spies, C., Li, K., Laaksonen, T., Auerbach, D., Jung, G., and Schneider, M. (2012) High photostability and enhanced fluorescence of gold nanoclusters by silver doping, *Nanoscale* 4, 7624-7631.
- [28] Jung, Y., Reif, R., Zeng, Y., and Wang, R. K. (2011) Three-dimensional high-resolution imaging of gold nanorods uptake in sentinel lymph nodes, *Nano Lett* 11, 2938-2943.
- [29] Lee, K. S., and El-Sayed, M. A. (2006) Gold and silver nanoparticles in sensing and imaging: sensitivity of plasmon response to size, shape, and metal composition, *J Phys Chem B* 110, 19220-19225.
- [30] Aslan, K., Zhang, J., Lakowicz, J. R., and Geddes, C. D. (2004) Saccharide sensing using gold and silver nanoparticles--a review, *J Fluoresc* 14, 391-400.
- [31] Tang, F., Li, L., and Chen, D. (2012) Mesoporous silica nanoparticles: synthesis, biocompatibility and drug delivery, *Adv Mater* 24, 1504-1534.
- [32] Zhao, Y., Trewyn, B. G., Slowing, II, and Lin, V. S. (2009) Mesoporous silica nanoparticle-based double drug delivery system for glucose-responsive controlled release of insulin and cyclic AMP, *J Am Chem Soc* 131, 8398-8400.
- [33] Yuan, Q., Hein, S., and Misra, R. D. (2010) New generation of chitosan-encapsulated ZnO quantum dots loaded with drug: synthesis, characterization and in vitro drug delivery response, *Acta Biomater* 6, 2732-2739.
- [34] Rasmussen, J. W., Martinez, E., Louka, P., and Wingett, D. G. (2010) Zinc oxide nanoparticles for selective destruction of tumor cells and potential for drug delivery applications, *Expert Opin Drug Deliv* 7, 1063-1077.
- [35] Nie, L., Gao, L., Feng, P., Zhang, J., Fu, X., Liu, Y., Yan, X., and Wang, T. (2006) Three-dimensional functionalized tetrapod-like ZnO nanostructures for plasmid DNA delivery, *Small* 2, 621-625.
- [36] Shen, W., Xiong, H., Xu, Y., Cai, S., Lu, H., and Yang, P. (2008) ZnO-poly(methyl methacrylate) nanobeads for enriching and desalting low-abundant proteins followed by directly MALDI-TOF MS analysis, *Anal Chem* 80, 6758-6763.
- [37] Sun, C., Fang, C., Stephen, Z., Veiseh, O., Hansen, S., Lee, D., Ellenbogen, R. G., Olson, J., and Zhang, M. (2008) Tumor-targeted drug delivery and MRI contrast

- enhancement by chlorotoxin-conjugated iron oxide nanoparticles, *Nanomedicine (Lond)* 3, 495-505.
- [38] Jain, T. K., Morales, M. A., Sahoo, S. K., Leslie-Pelecky, D. L., and Labhassetwar, V. (2005) Iron oxide nanoparticles for sustained delivery of anticancer agents, *Mol Pharm* 2, 194-205.
- [39] Gupta, A. K., and Gupta, M. (2005) Synthesis and surface engineering of iron oxide nanoparticles for biomedical applications, *Biomaterials* 26, 3995-4021.
- [40] Qin, Y., Sun, L., Li, X. X., Cao, Q. Q., Wang, H., Tang, X. F., and Ye, L. (2011) Highly water-dispersible TiO₂ nanoparticles for doxorubicin delivery: effect of loading mode on therapeutic efficacy, *Journal of Materials Chemistry* 21, 18003-18010.
- [41] Panyam, J., Zhou, W. Z., Prabha, S., Sahoo, S. K., and Labhassetwar, V. (2002) Rapid endo-lysosomal escape of poly(DL-lactide-co-glycolide) nanoparticles: implications for drug and gene delivery, *FASEB J* 16, 1217-1226.
- [42] Bhaw-Luximon, A., Meeram, L. M., Jugdawa, Y., Helbert, W., and Jhurry, D. (2011) Oligoagarose-g-polycaprolactone loaded nanoparticles for drug delivery applications, *Polym Chem-Uk* 2, 77-79.
- [43] Guo, S., Huang, Y., Zhang, W., Wang, W., Wei, T., Lin, D., Xing, J., Deng, L., Du, Q., Liang, Z., Liang, X. J., and Dong, A. (2011) Ternary complexes of amphiphilic polycaprolactone-graft-poly (N,N-dimethylaminoethyl methacrylate), DNA and polyglutamic acid-graft-poly(ethylene glycol) for gene delivery, *Biomaterials* 32, 4283-4292.
- [44] Damascelli, B., Patelli, G. L., Lanocita, R., Di Tolla, G., Frigerio, L. F., Marchiano, A., Garbagnati, F., Spreafico, C., Ticha, V., Gladin, C. R., Palazzi, M., Crippa, F., Oldini, C., Calo, S., Bonaccorsi, A., Mattavelli, F., Costa, L., Mariani, L., and Cantu, G. (2003) A novel intraarterial chemotherapy using paclitaxel in albumin nanoparticles to treat advanced squamous cell carcinoma of the tongue: preliminary findings, *AJR Am J Roentgenol* 181, 253-260.
- [45] Dyer, A. M., Hinchcliffe, M., Watts, P., Castile, J., Jabbal-Gill, I., Nankervis, R., Smith, A., and Illum, L. (2002) Nasal delivery of insulin using novel chitosan based formulations: a comparative study in two animal models between simple chitosan formulations and chitosan nanoparticles, *Pharm Res* 19, 998-1008.
- [46] Huang, M., Khor, E., and Lim, L. Y. (2004) Uptake and cytotoxicity of chitosan molecules and nanoparticles: effects of molecular weight and degree of deacetylation, *Pharm Res* 21, 344-353.
- [47] Kaul, G., and Amiji, M. (2002) Long-circulating poly(ethylene glycol)-modified gelatin nanoparticles for intracellular delivery, *Pharm Res* 19, 1061-1067.
- [48] Cascone, M. G., Lazzeri, L., Carmignani, C., and Zhu, Z. (2002) Gelatin nanoparticles produced by a simple W/O emulsion as delivery system for methotrexate, *J Mater Sci Mater Med* 13, 523-526.
- [49] Sarmiento, B., Ribeiro, A., Veiga, F., Sampaio, P., Neufeld, R., and Ferreira, D. (2007) Alginate/chitosan nanoparticles are effective for oral insulin delivery, *Pharm Res* 24, 2198-2206.
- [50] You, J. O., Liu, Y. C., and Peng, C. A. (2006) Efficient gene transfection using chitosan-alginate core-shell nanoparticles, *Int J Nanomedicine* 1, 173-180.
- [51] Ahmad, Z., Pandey, R., Sharma, S., and Khuller, G. K. (2006) Alginate nanoparticles as antituberculosis drug carriers: formulation development, pharmacokinetics and therapeutic potential, *Indian J Chest Dis Allied Sci* 48, 171-176.
- [52] Nel, A. E., Mädler, L., Velegol, D., Xia, T., Hoek, E. M. V., Somasundaran, P., Klaessig, F., Castranova, V., and Thompson, M. (2009) Understanding biophysicochemical interactions at the nano-bio interface, *Nature Materials* 8, 543-557.
- [53] Hillaireau, H., and Couvreur, P. (2009) Nanocarriers' entry into the cell: Relevance to drug delivery, *Cellular and Molecular Life Sciences* 66, 2873-2896.

- [54] Aderem, A., and Underhill, D. M. (1999) Mechanisms of phagocytosis in macrophages, *Annu Rev Immunol* 17, 593-623.
- [55] Korn, E. D., and Weisman, R. A. (1967) Phagocytosis of latex beads by *Acanthamoeba*. II. Electron microscopic study of the initial events, *J Cell Biol* 34, 219-227.
- [56] Schafer, V., von Briesen, H., Andreesen, R., Steffan, A. M., Royer, C., Troster, S., Kreuter, J., and Rubsamen-Waigmann, H. (1992) Phagocytosis of nanoparticles by human immunodeficiency virus (HIV)-infected macrophages: a possibility for antiviral drug targeting, *Pharm Res* 9, 541-546.
- [57] Tabata, Y., and Ikada, Y. (1988) Effect of the size and surface charge of polymer microspheres on their phagocytosis by macrophage, *Biomaterials* 9, 356-362.
- [58] Devine, D. V., Wong, K., Serrano, K., Chonn, A., and Cullis, P. R. (1994) Liposome-complement interactions in rat serum: implications for liposome survival studies, *Biochim Biophys Acta* 1191, 43-51.
- [59] Chonn, A., Cullis, P. R., and Devine, D. V. (1991) The role of surface charge in the activation of the classical and alternative pathways of complement by liposomes, *J Immunol* 146, 4234-4241.
- [60] Couvreur, P., and Vauthier, C. (2006) Nanotechnology: intelligent design to treat complex disease, *Pharm Res* 23, 1417-1450.
- [61] Betageri, G. V., Black, C. D., Szebeni, J., Wahl, L. M., and Weinstein, J. N. (1993) Fc-receptor-mediated targeting of antibody-bearing liposomes containing dideoxycytidine triphosphate to human monocyte/macrophages, *J Pharm Pharmacol* 45, 48-53.
- [62] Conner, S. D., and Schmid, S. L. (2003) Regulated portals of entry into the cell, *Nature* 422, 37-44.
- [63] Anderson, R. G. (1998) The caveolae membrane system, *Annu Rev Biochem* 67, 199-225.
- [64] Mayor, S., and Pagano, R. E. (2007) Pathways of clathrin-independent endocytosis, *Nat Rev Mol Cell Biol* 8, 603-612.
- [65] Bareford, L. M., and Swaan, P. W. (2007) Endocytic mechanisms for targeted drug delivery, *Adv Drug Deliv Rev* 59, 748-758.
- [66] Swanson, J. A., and Watts, C. (1995) Macropinocytosis, *Trends Cell Biol* 5, 424-428.
- [67] Oh, E., Delehanty, J. B., Sapsford, K. E., Susumu, K., Goswami, R., Blanco-Canosa, J. B., Dawson, P. E., Granek, J., Shoff, M., Zhang, Q., Goering, P. L., Huston, A., and Medintz, I. L. (2011) Cellular Uptake and Fate of PEGylated Gold Nanoparticles Is Dependent on Both Cell-Penetration Peptides and Particle Size, *ACS Nano* 5, 6434-6448.
- [68] Cho, E. C., Zhang, Q., and Xia, Y. (2011) The effect of sedimentation and diffusion on cellular uptake of gold nanoparticles, *Nat Nanotechnol* 6, 385-391.
- [69] Albanese, A., and Chan, W. C. (2011) Effect of gold nanoparticle aggregation on cell uptake and toxicity, *ACS Nano* 5, 5478-5489.
- [70] Wang, Z., Zhang, J., Ekman, J. M., Kenis, P. J., and Lu, Y. (2010) DNA-mediated control of metal nanoparticle shape: one-pot synthesis and cellular uptake of highly stable and functional gold nanoflowers, *Nano Lett* 10, 1886-1891.
- [71] Cho, E. C., Au, L., Zhang, Q., and Xia, Y. (2010) The effects of size, shape, and surface functional group of gold nanostructures on their adsorption and internalization by cells, *Small* 6, 517-522.
- [72] Brandenberger, C., Mühlfeld, C., Ali, Z., Lenz, A. G., Schmid, O., Parak, W. J., Gehr, P., and Rothen-Rutishauser, B. (2010) Quantitative evaluation of cellular uptake and trafficking of plain and polyethylene glycol-coated gold nanoparticles, *Small* 6, 1669-1678.

- [73] Mandal, D., Maran, A., Yaszemski, M. J., Bolander, M. E., and Sarkar, G. (2009) Cellular uptake of gold nanoparticles directly cross-linked with carrier peptides by osteosarcoma cells, *Journal of Materials Science: Materials in Medicine* 20, 347-350.
- [74] Chithrani, B. D., Stewart, J., Allen, C., and Jaffray, D. A. (2009) Intracellular uptake, transport, and processing of nanostructures in cancer cells, *Nanomed-Nanotechnol* 5, 118-127.
- [75] Nativo, P., Prior, I. A., and Brust, M. (2008) Uptake and intracellular fate of surface-modified gold nanoparticles, *ACS Nano* 2, 1639-1644.
- [76] Zhang, W., Tong, L., and Yang, C. (2012) Cellular binding and internalization of functionalized silicon nanowires, *Nano Lett* 12, 1002-1006.
- [77] Kim, J. A., Aberg, C., Salvati, A., and Dawson, K. A. (2012) Role of cell cycle on the cellular uptake and dilution of nanoparticles in a cell population, *Nat Nanotechnol* 7, 62-68.
- [78] Rejman, J., Oberle, V., Zuhorn, I. S., and Hoekstra, D. (2004) Size-dependent internalization of particles via the pathways of clathrin- and caveolae-mediated endocytosis, *Biochem J* 377, 159-169.
- [79] Zhang, Y., So, M. K., and Rao, J. (2006) Protease-modulated cellular uptake of quantum dots, *Nano Lett* 6, 1988-1992.
- [80] Gratton, S. E., Ropp, P. A., Pohlhaus, P. D., Luft, J. C., Madden, V. J., Napier, M. E., and DeSimone, J. M. (2008) The effect of particle design on cellular internalization pathways, *Proc Natl Acad Sci U S A* 105, 11613-11618.
- [81] Cartiera, M. S., Johnson, K. M., Rajendran, V., Caplan, M. J., and Saltzman, W. M. (2009) The uptake and intracellular fate of PLGA nanoparticles in epithelial cells, *Biomaterials* 30, 2790-2798.
- [82] Giljohann, D. A., Seferos, D. S., Daniel, W. L., Massich, M. D., Patel, P. C., and Mirkin, C. A. (2010) Gold nanoparticles for biology and medicine, *Angew Chem Int Ed Engl* 49, 3280-3294.
- [83] Sperling, R. A., Rivera gil, P., Zhang, F., Zanella, M., and Parak, W. J. (2008) Biological applications of gold nanoparticles, *Chemical Society Reviews* 37, 1896-1908.
- [84] Hutchings, G. J., Brust, M., and Schmidbaur, H. (2008) Gold - an introductory perspective, *Chemical Society Reviews* 37, 1759-1765.
- [85] Wang, H., Huff, T. B., Zweifel, D. A., He, W., Low, P. S., Wei, A., and Cheng, J. X. (2005) In vitro and in vivo two-photon luminescence imaging of single gold nanorods, *Proc Natl Acad Sci U S A* 102, 15752-15756.
- [86] Raschke, G., Kowarik, S., Franzl, T., Sonnichsen, C., Klar, T. A., Feldmann, J., Nichtl, A., and Kurzinger, K. (2003) Biomolecular recognition based on single gold nanoparticle light scattering, *Nano Letters* 3, 935-938.
- [87] Manju, S., and Sreenivasan, K. (2012) Gold nanoparticles generated and stabilized by water soluble curcumin-polymer conjugate: blood compatibility evaluation and targeted drug delivery onto cancer cells, *J Colloid Interface Sci* 368, 144-151.
- [88] McMahon, K. M., Mutharasan, R. K., Tripathy, S., Veliceasa, D., Bobeica, M., Shumaker, D. K., Luthi, A. J., Helfand, B. T., Ardehali, H., Mirkin, C. A., Volpert, O., and Thaxton, C. S. (2011) Biomimetic high density lipoprotein nanoparticles for nucleic acid delivery, *Nano Lett* 11, 1208-1214.
- [89] Tripp, S. L., Kim, B., and Wei, A. (2002) TEM image analysis of self-organized large gold nanoparticle arrays, *Microscopy and Microanalysis* 8, 1134-1135.
- [90] Lippitz, M., van Dijk, M. A., and Orrit, M. (2005) Third-harmonic generation from single gold nanoparticles, *Nano Lett* 5, 799-802.
- [91] Asahi, T., Lluit, G., Tanaka, G., Uwada, T., and Masuhara, H. (2009) Spectral and 3-Dimensional Tracking of Single Gold Nanoparticles in Living Cells Studied by Rayleigh Light Scattering Microscopy, *Journal of Physical Chemistry C* 113, 11766-11772.

- [92] Butet, J., Duboisset, J., Bachelier, G., Russier-Antoine, I., Benichou, E., Jonin, C., and Brevet, P. F. (2010) Optical second harmonic generation of single metallic nanoparticles embedded in a homogeneous medium, *Nano Lett* 10, 1717-1721.
- [93] Kumar, S., Harrison, N., Richards-Kortum, R., and Sokolov, K. (2007) Plasmonic nanosensors for imaging intracellular biomarkers in live cells, *Nano Letters* 7, 1338-1343.
- [94] Steiner, M., Debus, C., Failla, A. V., and Meixner, A. J. (2008) Plasmon-enhanced emission in gold nanoparticle aggregates, *Journal of Physical Chemistry C* 112, 3103-3108.
- [95] Imura, K., Nagahara, T., and Okamoto, H. (2004) Plasmon mode imaging of single gold nanorods, *J Am Chem Soc* 126, 12730-12731.
- [96] Klar, T., Perner, M., Grosse, S., von Plessen, G., Spirkl, W., and Feldmann, J. (1998) Surface-plasmon resonances in single metallic nanoparticles, *Physical Review Letters* 80, 4249-4252.
- [97] Mooradian, A. (1969) Photoluminescence of Metals, *Physical Review Letters* 22, 185-187.
- [98] Eichelbaum, M., Schmidt, B. E., Ibrahim, H., and Rademann, K. (2007) Three-photon-induced luminescence of gold nanoparticles embedded in and located on the surface of glassy nanolayers, *Nanotechnology* 18, -.
- [99] Farrer, R. A., Butterfield, F. L., Chen, V. W., and Fourkas, J. T. (2005) Highly efficient multiphoton-absorption-induced luminescence from gold nanoparticles, *Nano Lett* 5, 1139-1142.
- [100] Durr, N. J., Larson, T., Smith, D. K., Korgel, B. A., Sokolov, K., and Ben-Yakar, A. (2007) Two-photon luminescence imaging of cancer cells using molecularly targeted gold nanorods, *Nano Letters* 7, 941-945.
- [101] So, P. T. C. (2001) Two-photon Fluorescence Light Microscopy, In *eLS*, John Wiley & Sons, Ltd.
- [102] Turkevich, J., Stevenson, P. C., and Hillier, J. (1951) A study of the nucleation and growth processes in the synthesis of colloidal gold, *Discussions of the Faraday Society* 11, 55-75.
- [103] Frens, G. (1972) Particle-Size and Sol Stability in Metal Colloids, *Kolloid Z Z Polym* 250, 736-8.
- [104] Brown, K. R., and Natan, M. J. (1998) Hydroxylamine seeding of colloidal Au nanoparticles in solution and on surfaces, *Langmuir* 14, 726-728.
- [105] Berg, M. J., Sorensen, C. M., and Chakrabarti, A. (2005) Patterns in Mie scattering: evolution when normalized by the Rayleigh cross section, *Appl Opt* 44, 7487-7493.
- [106] Zhang, S. M., Zhu, B., Zhou, S. F., Xu, S. Q., and Qiu, J. R. (2007) Multi-photon absorption upconversion luminescence of a Tb³⁺-doped glass excited by an infrared femtosecond laser, *Optics Express* 15, 6883-6888.
- [107] Boyd, G. T., Yu, Z. H., and Shen, Y. R. (1986) Photoinduced luminescence from the noble metals and its enhancement on roughened surfaces, *Phys Rev B Condens Matter* 33, 7923-7936.
- [108] Das, S. K., Bock, M., O'Neill, C., Grunwald, R., Lee, K. M., Lee, H. W., Lee, S., and Rotermund, F. (2008) Efficient second harmonic generation in ZnO nanorod arrays with broadband ultrashort pulses, *Applied Physics Letters* 93.
- [109] Labouta, H. I., Liu, D. C., Lin, L. L., Butler, M. K., Grice, J. E., Raphael, A. P., Kraus, T., El-Khordagui, L. K., Soyer, H. P., Roberts, M. S., Schneider, M., and Prow, T. W. (2011) Gold nanoparticle penetration and reduced metabolism in human skin by toluene, *Pharm Res* 28, 2931-2944.
- [110] Labouta, H. I., Kraus, T., El-Khordagui, L. K., and Schneider, M. (2011) Combined multiphoton imaging-pixel analysis for semiquantitation of skin penetration of gold nanoparticles, *Int J Pharm* 413, 279-282.

- [111] Labouta, H. I., el-Khordagui, L. K., Kraus, T., and Schneider, M. (2011) Mechanism and determinants of nanoparticle penetration through human skin, *Nanoscale* 3, 4989-4999.
- [112] Chithrani, B. D., Ghazani, A. A., and Chan, W. C. W. (2006) Determining the size and shape dependence of gold nanoparticle uptake into mammalian cells, *Nano Letters* 6, 662-668.
- [113] Jiang, W., Kim, B. Y., Rutka, J. T., and Chan, W. C. (2008) Nanoparticle-mediated cellular response is size-dependent, *Nat Nanotechnol* 3, 145-150.
- [114] Chithrani, B. D., and Chan, W. C. (2007) Elucidating the mechanism of cellular uptake and removal of protein-coated gold nanoparticles of different sizes and shapes, *Nano Lett* 7, 1542-1550.
- [115] Dash, B. C., Rethore, G., Monaghan, M., Fitzgerald, K., Gallagher, W., and Pandit, A. (2010) The influence of size and charge of chitosan/polyglutamic acid hollow spheres on cellular internalization, viability and blood compatibility, *Biomaterials* 31, 8188-8197.
- [116] Arnida, Malugin, A., and Ghandehari, H. (2010) Cellular uptake and toxicity of gold nanoparticles in prostate cancer cells: a comparative study of rods and spheres, *Journal of Applied Toxicology* 30, 212-217.
- [117] Levy, R., Shaheen, U., Cesbron, Y., and See, V. (2010) Gold nanoparticles delivery in mammalian live cells: a critical review, *Nano Rev* 1.
- [118] Alkilany, A. M., and Murphy, C. J. (2010) Toxicity and cellular uptake of gold nanoparticles: what we have learned so far?, *J Nanopart Res* 12, 2313-2333.
- [119] Eychmuller, A., and Ziegler, C. (2011) Seeded Growth Synthesis of Uniform Gold Nanoparticles with Diameters of 15-300 nm, *Journal of Physical Chemistry C* 115, 4502-4506.
- [120] Yu, C., Varghese, L., and Irudayaraj, J. (2007) Surface modification of cetyltrimethylammonium bromide-capped gold nanorods to make molecular probes, *Langmuir* 23, 9114-9119.
- [121] Tong, L., He, W., Zhang, Y., Zheng, W., and Cheng, J. X. (2009) Visualizing systemic clearance and cellular level biodistribution of gold nanorods by intrinsic two-photon luminescence, *Langmuir* 25, 12454-12459.
- [122] Haiss, W., Thanh, N. T., Aveyard, J., and Fernig, D. G. (2007) Determination of size and concentration of gold nanoparticles from UV-vis spectra, *Anal Chem* 79, 4215-4221.
- [123] Diaspro, A. (2002) *Confocal and two-photon microscopy : foundations, applications, and advances*, Wiley-Liss, New York.
- [124] Cho, E. C., Liu, Y., and Xia, Y. N. (2010) A Simple Spectroscopic Method for Differentiating Cellular Uptakes of Gold Nanospheres and Nanorods from Their Mixtures, *Angew Chem Int Edit* 49, 1976-1980.

ABBREVIATIONS

AFM	atomic force microscopy
ATP	adenosine triphosphate
AuNPs	gold nanoparticles
BD	biodistribution
CME	clathrin-mediated endocytosis
CvME	caveolae-mediated endocytosis
DDS	drug delivery system
DNA	deoxyribonucleic acid
FWHM	full width of half maximum
LSPR	localized surface Plasmon resonance
MAIL	multiphoton absorption induced luminescence
MP-LSM	multiphoton laser scanning microscopy
NA	numerical aperture
NPs	nanoparticles
PEG	polyethylene glycol
PK	pharmacokinetics
PLGA	poly(D,L-lactic-co-glycolic acid)
PSF	point spread function
RES	reticuloendothelial system
SEM	scanning electron microscopy
SERS	surface-enhanced Raman scattering microscopy
SHG	second harmonic generation
SPT	single particle tracking
S/N	signal to noise ratio
TAIL	two photon absorption induced luminescence

Abbreviations

TEM	transmission electron microscopy
THG	third harmonic generation
UV/Vis	Ultraviolet-visible spectroscopy
λ_{ex}	excitation wavelength
λ_{em}	emission wavelength
ZnO NPs	Zinc oxide nanoparticles

CURRICULUM VITAE

Name Ke Li

Date of birth 11th November 1978

Place of birth Wei Nan, PR. China

Nationality Chinese

E-mail k.li@mx.uni-saarland.de
like988021@yahoo.cn

Education:

2005-2008: MSc. at the Department of Pharmaceutics, Faculty of Pharmacy, Tongji Medical College, Huazhong University of Science and Technology, PR.China. The thesis was entitled: 'Study on the Pharmacokinetics of APIC in Animals and Preparation of APIC Solid Dispersion Enteric-coated Capsules'.

1998-2002: BSc of pharmacy sciences, Faculty of Pharmacy, Xi An Jiaotong University, PR.China

1998: Completed high school at XI AN YuanDong High School, Xi An, China

Career Summary:

2008-present: Ph D candidate at Department of Pharmaceutical Nanotechnology, Saarland University, Saarbrücken, Germany

2002-2005: A licensed pharmacist at Faculty of Pharmacy, the First Hospital of XI AN Jiaotong University, PR.China.

Publications:

Research articles:

Li K, Schneider M., Visualization and discrimination of colloidal gold based on multiphoton laser scanning microscopy, *Journal of Physical Chemistry C* **in submission**.

Le Guevel X, Trouillet V, Spies C, **Li K**, Laaksonen T, Auerbach D, Jung G, Schneider M. High photostability and enhanced fluorescence of gold nanoclusters by silver doping. *Nanoscale* 2012;4(24):7624-31.

Poster presentations:

Li K, Schneider M., The wavelength dependence of the luminescence for different sized AuNP by 2-Photon CLSM, 7th European Biophysics Congress July 11-15th 2009 in Genova, Italy.

Li K, Schneider M., The use of commercial multiphoton-LSM for visualization and discrimination of the spherical gold nanoparticles, Controlled Release Society Annual Meeting, March 15-16th 2011, Jena, Germany

ACKNOWLEDGEMENTS

I would like to gratefully and sincerely thank Prof. Dr. Marc Schneider for his guidance, understanding, and patience during my graduate studies at Universität des Saarlandes. His kindness, helpfulness, stimulating suggestions, and constant encouragements helped me in all the time of my research and writing of this dissertation.

My special appreciation goes to all of my colleagues from the research group: Qiong Lian, Mardiyanto, Dr. Hagar Larbouta, Dr. Noha Nafee, Clemens Tscheka, Daniel Primavešy, Saeed Ahmad Khan, René Rietscher, Nazende Günday Türeli, Asli Katkiliç. I really enjoy the time with them. I have learned many from them as well.

Thanks go to those who provided me with technical supports, including: Dr Nico Reum, Petra König, Leon Muijs, Dr Brigitta Loretz and Dr Nicole Daum. Many thanks also to our office manager Ms. Karin Groß.

My special thanks would also goes to my beloved parents for their loving considerations and great confidence in me all through these years. Especially, I would like to give my special thanks to my wife Rui Meng whose patient love enabled me to complete this work.

Finally, financial supports from Universität des Saarlandes and Chinese Scholarship Council are gratefully acknowledged.

Ke Li

Saarbrücken

07. December 2012